Journal Pre-proof

In-situ vaccination using dual responsive organelle targeted nanoreactors

Vishnu Sunil, Anbu Mozhi, Wenbo Zhan, Jia Heng Teoh, Pramila Baban Ghode, Nitish V. Thakor, Chi-Hwa Wang

PII: S0142-9612(22)00483-5

DOI: https://doi.org/10.1016/j.biomaterials.2022.121843

Reference: JBMT 121843

To appear in: *Biomaterials*

Received Date: 2 July 2022

Revised Date: 20 September 2022

Accepted Date: 29 September 2022

Please cite this article as: Sunil V, Mozhi A, Zhan W, Teoh JH, Ghode PB, Thakor NV, Wang C-H, In-situ vaccination using dual responsive organelle targeted nanoreactors, *Biomaterials* (2022), doi: https://doi.org/10.1016/j.biomaterials.2022.121843.

Credit Author Statement

Vishnu Sunil: Conceptualization, Methodology, Investigation, Data Curation, Writing – Original Draft. Anbu Mozhi: Conceptualization, Methodology, Investigation, Data Curation. Wenbo Zhan: Methodology, Formal Analysis, Investigation. Jia Heng Teoh: Methodology, Investigation (3D printing). Pramila Baban Ghode: Methodology (In-vivo experiments). Nitish Thakor: Methodology (In-vivo experiments). Chi-Hwa Wang – Conceptualization, Supervision, Writing – Review and Editing, Funding Acquisition.

In-situ Vaccination Using Dual Responsive Organelle Targeted Nanoreactors

Vishnu Sunil[1†], Anbu Mozhi[1†], Wenbo Zhan[2], Jia Heng Teoh[1], Pramila Baban Ghode[3], Nitish V. Thakor[3,4], Chi-Hwa Wang[1]*

[1]Department of Chemical and Biomolecular Engineering, National University of Singapore, 4 Engineering Drive 4, Singapore 117585, Singapore

[2]School of Engineering, King's College, University of Aberdeen, Aberdeen AB24 3UE, UK

[3]Singapore Institute for Neurotechnology (SINAPSE), National University of Singapore, 28 Medical Drive, Singapore 117456, Singapore

[4]Department of Biomedical Engineering, Johns Hopkins School of Medicine, Baltimore, MD, United States

[†]These authors contributed equally to this work.

[*]Corresponding Author:

Email: chewch@nus.edu.sg (C.H. Wang)

Submitted to Biomaterials

September 2022

1. Keywords

In-situ vaccine, dual-responsive, backbone shattering, combination therapy, orthotopic glioblastoma mice model, personalized medicine.

2. Abstract

The poor translation of nanomedicines from bench to bedside can be attributed to (i) lack of a delivery system with precise drug compositions with no batch-to-batch variations, (ii) off-target or undesirable release of payload, and (iii) lack of a method to monitor the fate of the specific drug of interest, which often has to be modified with a fluorescent tag or replaced with a model drug which can be tracked. To overcome these translation hurdles, we developed dual responsive organelle targeted nanoreactors (DRONEs) with precise drug composition, site specific payload release and which enable accurate in-vivo monitoring. DRONEs consist of a polyprodrug inner core composed of a dual responsive backbone containing a photosensitizer (Protoporphyrin IX) grafted with functionalized polyethylene glycol (PEG) outer shell to prolong blood circulation and a tumour homing pro-apoptotic peptide ($CGKRK_D[KLAKLAK]_2$) (THP). DRONEs can significantly reduce the tumour burden in an orthotopic glioblastoma model due to its BBB penetrating and tumour homing capabilities. DRONEs exhibit good safety profile and biocompatibility along with a reliable route of elimination. DRONEs showed great potential as an in-situ vaccine which can not only eliminate the tumour but also trigger an adaptive immune response which would provide long-term anti-tumoural immunity.

3. Graphical Abstract

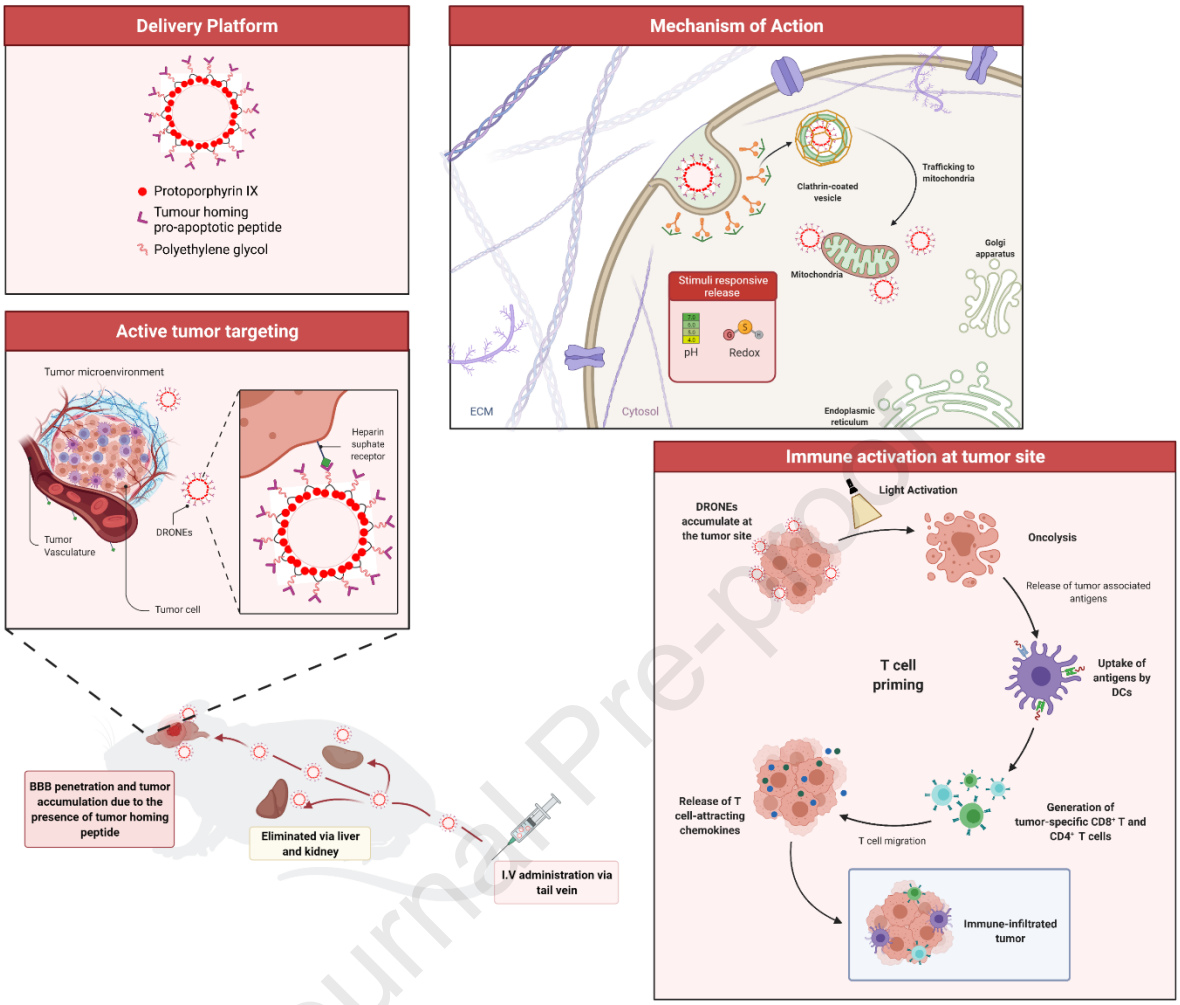

4. Introduction

Nanoparticle based therapeutics such as micelles[1], liposomes[2] and dendrimers[3] have gained clinical relevance over the last two decades due to their ability in enhancing the therapeutic index of potent anti-cancer drugs either by improving therapeutic efficacy or reducing systemic toxicity[4]. Since the US Food and Drug Administration (FDA) and European Medical Agency (EMA)'s approval of the pioneering nano-drug formulations such as Doxil (liposomal doxorubicin) and Abraxane (albumin-particle bound paclitaxel), several newer generation nanosystems such as VYXEOS (combination chemotherapy nanoparticle) and Patisiran/ONPATTRO (siRNA-delivering lipid-based nanoparticle) capable of delivering multiple highly challenging therapeutics, have been developed[5]. However, since 1995, only ~20 nanopharmaceuticals have been approved/likely to be approved for oncology indications, which is incommensurate to the amount of money and time spent in the development of nanodrugs since Doxil[6]. The translation of innovative delivery systems to the clinic has three key challenges – batch-batch variation in drug composition within the carrier[7], premature or unsynchronized release of drugs during preparation, storage or in circulation, and lack of a method to monitor the fate of the specific drug in-vivo. To achieve precise drug compositions and uniform carrier architecture, polymer-drug conjugates, also known as polymeric prodrugs or polyprodrugs have been studied[8-10]. Polyprodrugs are developed by covalently tethering repeating prodrug units allowing precise drug content control through rational molecular design[11-13]. On-demand customizable release of the drugs from the prodrugs can be enabled using stimuli-responsive linkers such as hydrazine bonds[14, 15], thioketal bonds[16], or disulfide bonds[17], which allow the prodrugs to remain in a masked, inactive state under normal conditions but release the intact drug when triggered by a specific pathological milieu[18]. Moreover, therapeutic payloads and/or carriers are usually tagged with a fluorescent molecule to monitor the fate of the nanosystem using fluorescence imaging, heavy metal-based contrast agents for positron emission tomography (PET), magnetic resonance imaging (MRI) or CT imaging and recently upconversion imaging[19-21]. However, these methods using a modified form of the drug or similar model drugs, do not paint an accurate picture of the biodistribution of the specific drug of interest.

Polyprodrugs are excellent candidates to achieve combination therapies due to their ability to incorporate multiple therapeutics within their backbone[22-25]. Nowadays, combination therapies are more commonly used in the clinic to leverage on their different mechanisms of action within their maximum tolerated dose. Among combination therapies, chemophototherapy has shown promise in achieving significant tumour reduction in pre-clinical studies[26]. For example, Carter et al. demonstrated significant prolonged survival (80% cure rate, median time of tumour regrowth – 90 days) in nude mice bearing subcutaneous tumours grown from the KB cancer cell line, using porphyrin-phospholipid (PoP) liposomes containing doxorubicin[27]. Similarly, an organoplatinum (II) metallacage exhibited superior tumour suppression in different types of in-vitro and in-vivo tumour models by combining a chemotherapeutic platinum drug and a porphyrin based photosensitizer[28]. However, clinical data show systemic toxicity and acquired drug resistance limits the long-term effectiveness of chemotherapeutic agents[29]. Moreover, myelosuppression associated with chemotherapeutics has a detrimental effect on the adaptive immune response, which is essential to prevent tumour reoccurrence[30, 31]. Therapeutic peptides, which trigger mitochondrial-dependent apoptosis with limited off-target toxicity and low occurrence of drug resistance, have been studied as potential alternatives to conventional chemotherapeutics[32-34]. On the other hand, photodynamic therapy (PDT) which involves the generation of reactive oxygen species in the presence of a photosensitizer, oxygen and light, can cause significant damage to lipids, DNA and protein resulting from changes in mitochondrial functions[35, 36]. The double-membrane-structured mitochondrion

has been explored as a therapeutic target due to its vital roles in cellular energy metabolism and apoptotic cell death and distinguishing structure and function between healthy cells and cancer cells. However, the limited diffusion and action range (10-20 nm) of the generated ROS limits the extent of mitochondrial oxidative stress exerted. Hence, it is essential to develop mitochondria targeted nanosystems to fully realize the therapeutic potential of PDT. Although combination therapies have shown promise in initial tumour reduction in pre-clinical and clinical trials, their immunomodulatory effects and therefore their ability to prevent tumour recurrence have rarely been studied. On the other hand, development of personalized vaccines based on neoantigens and immune checkpoint inhibitors has been researched for several years as a potential solution to prevent tumour recurrence. However, only one cell-based vaccine has been approved by the FDA to date, and the overall rate of clinical benefit is still low[37, 38]. The dismal clinical success of these vaccines can be attributed to the variability of tumour associated antigens (TAAs) due to the inter- and intra-tumour heterogenicity and immunosuppressive tumour microenvironments[39, 40]. Furthermore, these procedures are expensive, complex and only effective in small populations[41, 42]. Hence, we envisage an optimal therapeutic strategy would combine initial tumour reduction along with induction of anti-tumoural immunity to function as an in-situ vaccine.

In this work, we developed dual responsive organelle targeted nanoreactors (DRONEs) to function as an in-situ vaccine which can induce immunogenic cell death (ICD), enable release of TAAs, enhance antigen presentation and promote proliferation of cytotoxic T lymphocytes. DRONEs consist of (i) a polyprodrug inner core composed of a dual responsive backbone containing a photosensitizer (Protoporphyrin IX), (ii) functionalized polyethylene glycol (PEG) outer shell to prolong blood circulation, and (iii) a tumour homing pro-apoptotic peptide ($CGKRK_D[KLAKLAK]_2$) (THP).

As shown in Scheme 1, the tumour homing peptide enables DRONEs to selectively bind to tumour endothelial cells and tumour cells. Enhanced tumour penetration and internalization allows the DRONEs to accumulate within the mitochondria. The high concentration of glutathione (GSH) in the cytoplasm and the acidic environment enables on-demand release of the intact PpIX molecules and the cleaved pro-apoptotic peptide. The released PpIX when activated with a light at 630 nm enables tumour cell death through ICD, apoptosis, necrosis, and vascular damage. While, the peptide disrupts the mitochondrial membrane and initiates apoptotic cell death. The released TAAs can then activate the antigen presenting cells which migrate to the draining lymph node to enable the proliferation of cytotoxic T lymphocytes, thereby achieving anti-tumoural immunity.

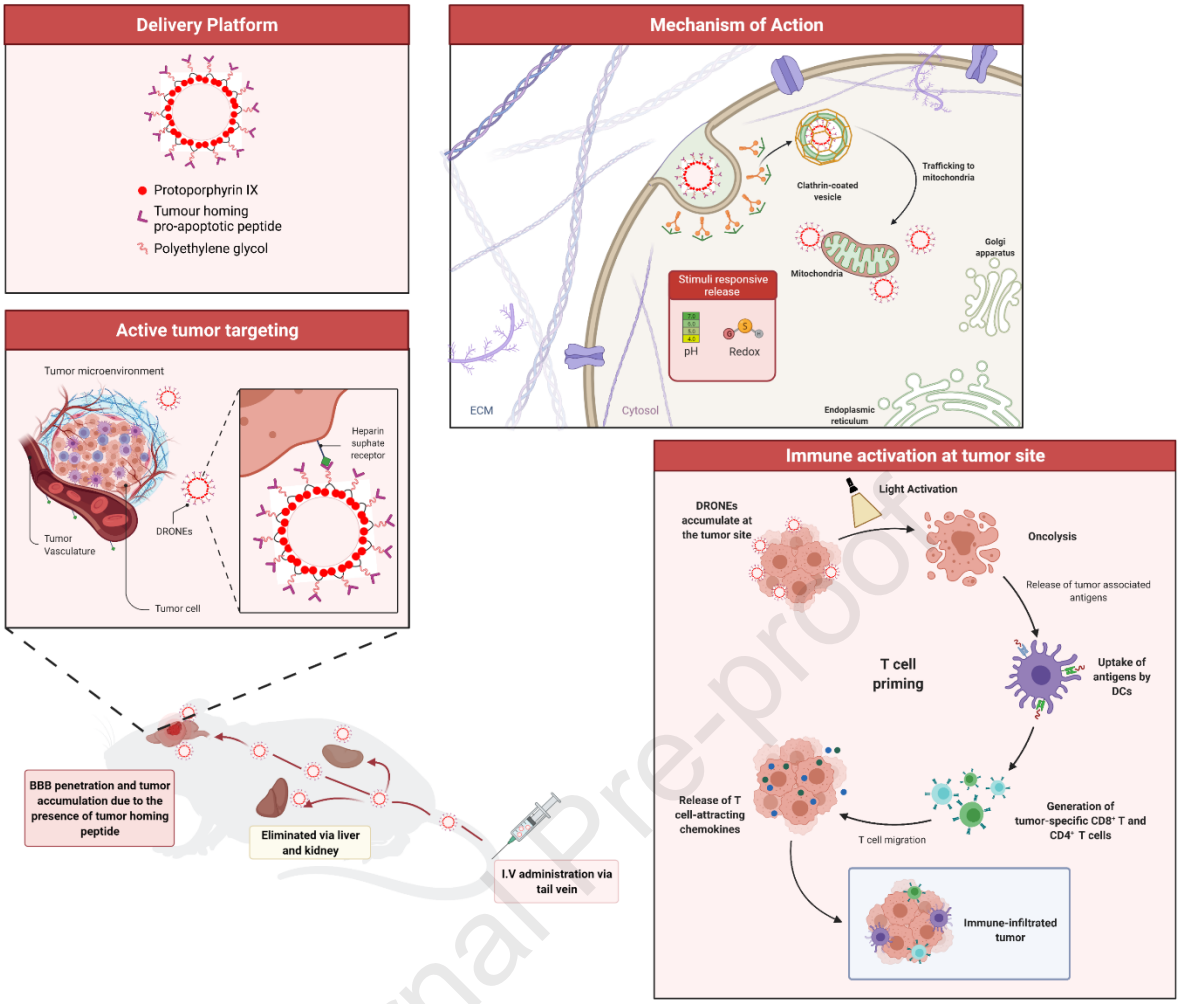

Scheme 1. Proposed mechanism of action of DRONEs as an in-situ vaccine.

5. Results and Discussion

5.1 Synthesis and Characterization of DRONEs

More evidence suggests the important role of the tumour microenvironment in oncogenesis, hence it is imperative to harness the pathophysiological differences between tumour tissues and healthy tissues to enable site specific activation of therapeutics[43]. The physiological characteristics that differentiate tumour cells from healthy cells are: (i) The elevated levels of GSH (~2-10 mM) associated with drug resistance and cancer pathology, is almost 10 times greater than that of normal cells, and (ii) The Warburg effect results in an acidic intracellular pH (pHi) of lysosomes ~5.0 and extracellular pH (pHe) in the TME ~6.5-6.8, compared to normal tissues ~ 7.2-7.4[44]. To leverage on these endogenous stimuli, we synthesized a dual responsive polyprodrug (DRP) by first polymerizing PpIX and cystamine dihydrochloride via condensation polymerization, followed by grafting with a pegylated tumour homing pro-apoptotic peptide (Scheme S1, Supporting Information). The fabricated DRP was systematically characterized using ^{1}H-NMR, FTIR and GPC to verify their chemical structure and molecular weight, respectively (Figure 1a) (Figure S1-7, Supporting Information). The number-average molecular weight (Mn) of DRP determined by GPC was 102.378 KDa (Mw/Mn = 1.46). DRONEs were then prepared by nanoprecipitation method. Dual responsive nanoreactors (DRNEs, without tumour homing pro-apoptotic peptide) was fabricated with using the same method. The mean conjugation percentage of PpIX and THP were calculated to be 47.19% and 28.47% using HPLC and Braford assay, respectively. Similarly, single responsive organelle targeted nanoreactors (SRONEs) were fabricated via the same process by replacing cystamine dihydrochloride in the backbone with ethylene diamine (EDA).

Both DRONEs and DRNEs can readily self-assemble in aqueous solutions forming translucent solutions with the photosensitizer in the core and polyethylene glycol in the corona (Figure 1b). The hydrodynamic diameter of DRNEs and DRONEs measured by DLS is 101.16 ± 0.43 nm and 123.29 ± 2.04 nm, respectively (Figure 1c). However, the TEM images of DRONEs suggest the formation of uniform spherical nanostructures with an average diameter circa ~80 nm (Figure 1d). The stretching capability of PEF in aqueous solutions could be the reason for the discrepancy in size distribution of DRONEs. After 14 days of incubation in α-MEM + 10% FBS media, DRONEs increase in size by ~20 nm (Figure 1e). DRNEs had a zeta potential of -13 ± 4.36 mV, whereas DRONEs had a surface charge of 32.54 ± 0.81 (Figure 1f). This increase in diameter and drastic change in zeta potential confirms the successful conjugation of the cationic THP to the polyprodrug. The UV-Vis absorbance spectra of DRONEs and DRNEs include the characteristic Soret band of PpIX at 401 nm and Q bands at 450-630 nm (Figure 1g). The PpIX within the backbone chain of DRONEs imparts a fluorescence maximum at 630 nm (Figure 1h). The ROS generation potential of DRONEs was evaluated by measuring the change in fluorescence intensity of Dichlorofluorescin (DCF) with respect to light exposure times (Figure 1i). The THP had a characteristic set of UV absorption bands in the far-UC CD spectrum region (<250 nm). The positive peak at ~193 nm and negative peaks at ~228 nm and ~208 nm suggest the peptide's α-helical formation. The identical CD spectra of DRONEs compared to that of the peptide proves that the grafting process had no effect on the activity of the peptide (Figure 1j).

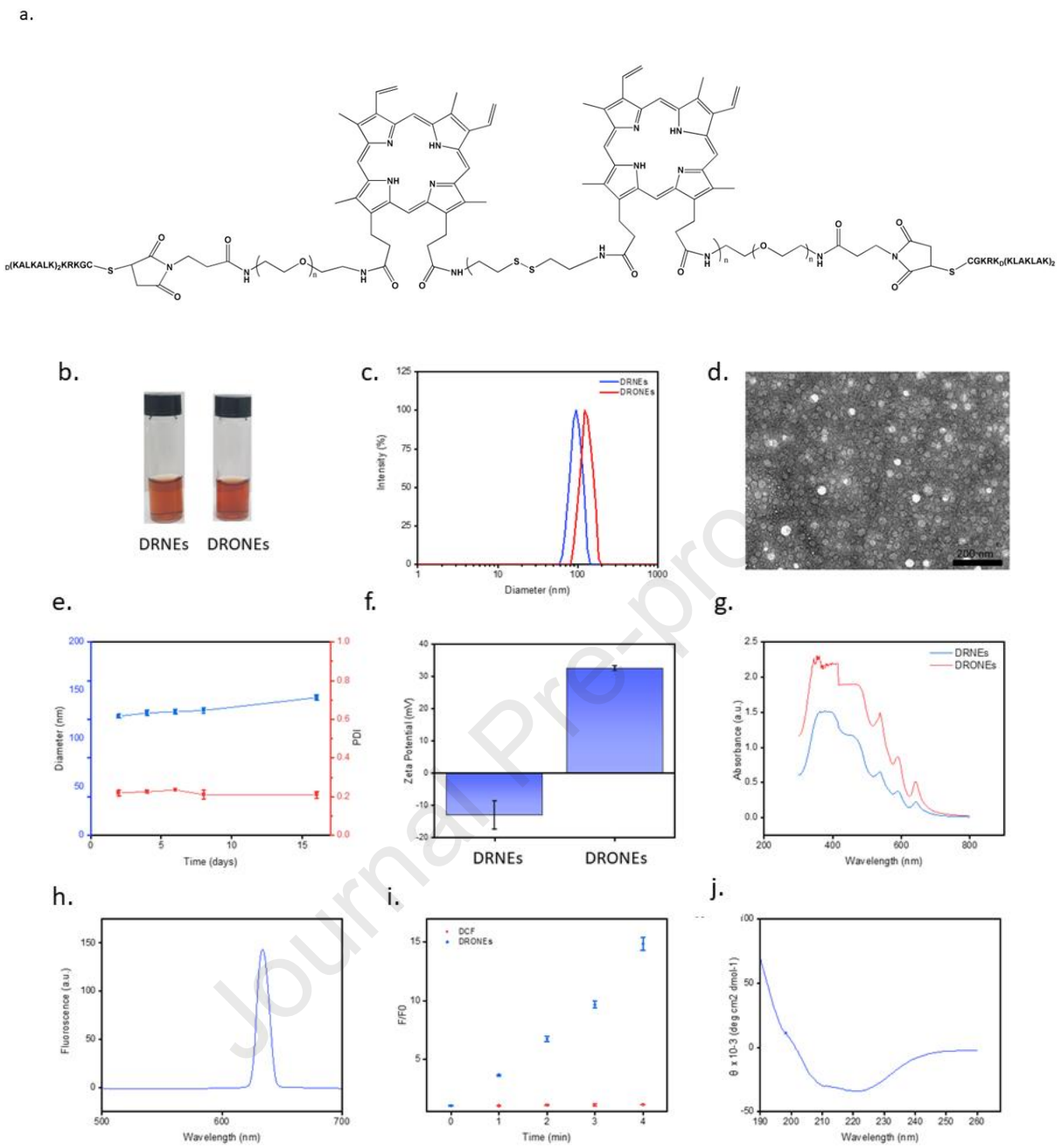

Figure 1. In-vitro characterization of DRONEs. a) Molecular structure of DRP, b) Images of the nanoparticle solutions, c) Hydrodynamic size distribution profile of IONs and BIONs, d) TEM image of DRONEs in PBS (Scale bar: 200 nm), e) Change in hydrodynamic diameter of DRONEs with respect to incubation time in α-MEM + 10% FBS media, f) Zeta potential of DRNEs and DRONEs, g) UV/Vis absorption spectrum of DRNEs and DRONEs, h) Fluorescence spectrum of DRONEs, i) ROS generation potential evaluated by fluorescence enhancement (F/F_0) as a function of light irradiation time (630 nm, 130 mW cm^{-2}), j) CD spectra of DRONEs. Error bars represent Mean ± SD ($n \geq 3$).

5.2 Dual responsive backbone shattering payload release

The site-specific rapid breakdown of the polyprodrug backbone is essential for optimum therapeutic efficacy. The proposed mechanism of the polyprodrug backbone shattering effect of intracellular levels of GSH and pH (Figure 2a) was studied using HPLC (Figure 2b). The release kinetics of DRONEs and SRONEs were evaluated at biologically relevant concentrations of GSH (0 and 10 mM) and pH conditions (7.4 and 5.0). The PpIX molecules remained intact at normal cell conditions (GSH – 0 mM, pH 7.4), however at typically tumour cell conditions (GSH – 10 mM, pH 5.0), 67.58 ± 3.29 % of PpIX was released at 24 h (Figure 2c). Even at neutral pH, in the presence of GSH, cleavage of the disulphide bond in the polyprodrug backbone chain results in 47.36 ± 5.27 % release of PpIX. On the other hand, the presence of GSH both at pH 5.0 and pH 7.4 has no effect on the release profile of SRONEs, whose disassembly mechanism is based on pH conditions (Figure 2d). Furthermore, over 24 h, in the presence of GSH, the size distribution of DRONEs first changed from a unimodal distribution with a peak at 120.85 ± 4.27 nm to a multimodal distribution with peaks at ~80 nm and ~400 nm before eventually breaking down into smaller particles of ~70 nm (Figure 2e). The representative dissociation process can be visualized using TEM (Figure 2f). In the presence of GSH, the gel permeation chromatography (GPC) curves of DRONEs widened over time, suggesting the presence of low molecular-weight species

(Figure 2g). This verifies that the reduction of the disulphide bond in the backbone of DRONEs is the driving force for rapid disassembly in a chain-shattering manner.

Figure 2. In-vitro study of dual responsive backbone shattering payload release. a) Proposed mechanism of redox and pH-triggered payload release, b) HPLC profiles of DRONEs in the

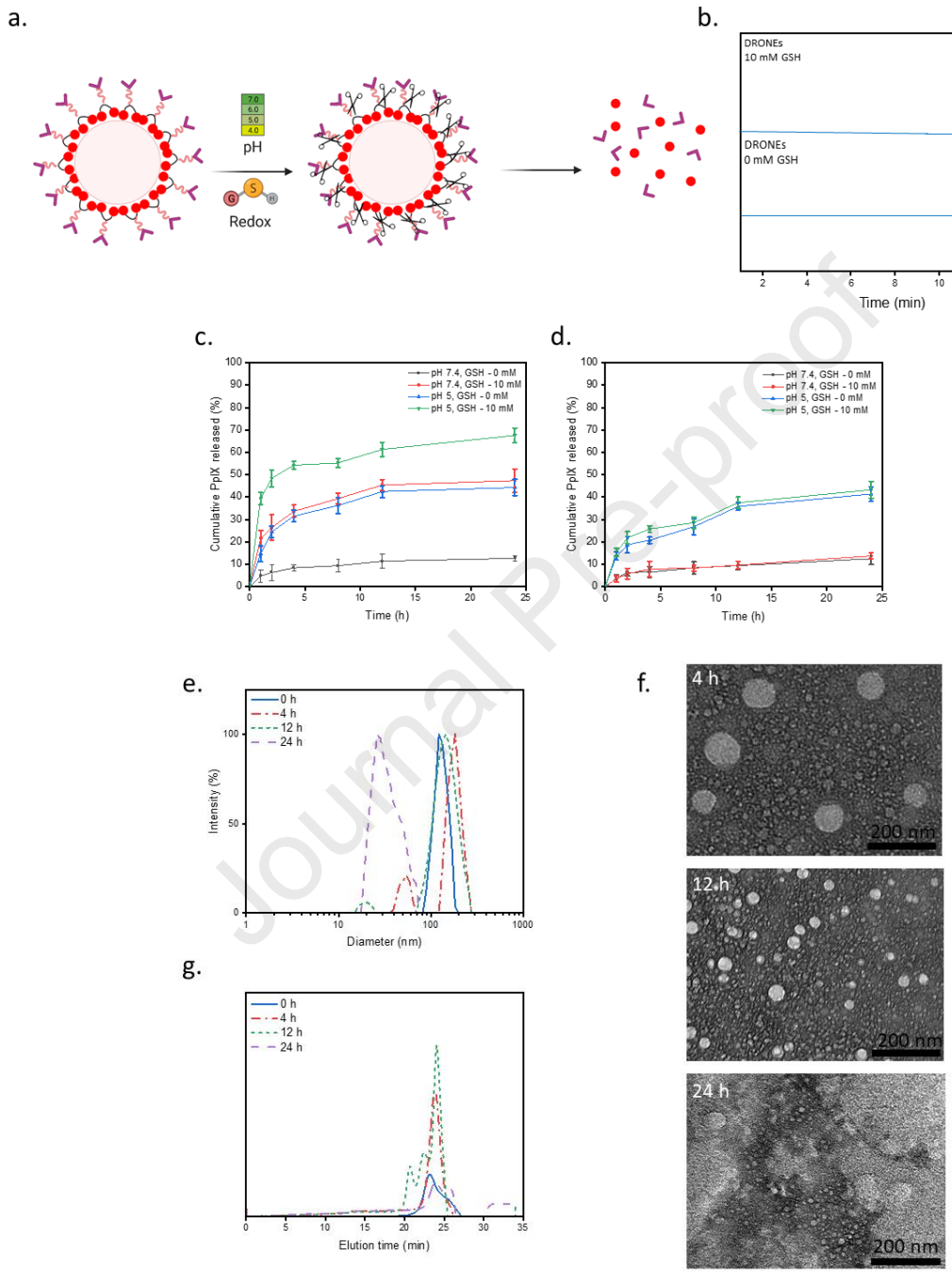

absence/presence of GSH, c) Redox and pH triggered PpIX release from DRONEs(cumulative % of total), d) Redox and pH triggered PpIX release from SRONEs(cumulative % of total), e) Change in hydrodynamic size with respect to incubation time (GSH – 10mM, pH 5.0), f) TEM images of DRONEs at different incubation times (GSH – 10mM, pH 5.0) (Scale bar: 200 nm), g) Change in GPC curves with respect to incubation time (GSH – 10mM, pH 5.0). Error bars represent Mean ± SD (n ≥ 3).

5.3 In-vitro evaluation of DRONEs in 3D printed mini-brains

We fabricated mini-brains as a potential alternative to conventional 2D monolayer and 3D spheroid models used to evaluate the efficacy of therapeutics. To mimic the orthotopic glioblastoma tumour model used in this study, a computer-aided design was reproduced by stacking mouse-macrophage (RAW 264.7) cells laden bio-ink via layer-by-layer deposition (Figure 3a) [45]. This physiologically relevant brain structure included a cavity at the right primary motor cortical region to house the bio-ink loaded U87 spheroids (~500 µm). This model is clinically relevant to transcriptomic and patient survival data as glioblastoma cells actively recruit macrophages and polarize them into glioblastoma-associated macrophages (GAMs) specific phenotype, thereby inducing glioblastoma cell progression, angiogenesis, and invasion.

The spheroids were excised to study the cytotoxicity of free PpIX, DRNEs, DRONEs with/without light irradiation (130 mW/cm^2, 5 mins) for 24 h at different concentrations (PpIX concentrations 0.25, 2.5 5,10,20,40 ug/ml) (Figure 3b and 3c). Free PpIX and DRNEs exhibited no toxicity to the U87 spheroids. Compared to groups treated with DRNEs and DRONEs, DRONEs + Light group significantly reduced the cell viability of U87 spheroids. The reduction in spheroid volume over 8 days was observed for the group treated with DRONEs + Light (Figure 3d). Furthermore, the cytotoxic effects of free PpIX, free THP, DRNEs, DRONEs with/without light was visualized using a Live/Dead assay (Figure 3e).

The photodynamic behavior of DRONEs on tumour cells was studied using a ROS detecting probe, 2',7'-Dichlorofluorescin diacetate (DCFH-DA). Only the group treated with DRONEs + Light showed strong green fluorescence, which suggests the ability to achieve localized ROS generation using irradiation (Figure S8, Supporting Information).

JC-1 assay was used to study the effect of free PpIX, free THP, DRNEs and DRONEs with/without light on the mitochondrial membrane potential. DRONEs + Light showed strong green fluorescence and negligible red fluorescence, comparable to the positive control group, however, DRNEs + Light exhibited both green fluorescence and red fluorescence, suggesting that its mitochondrial membrane depolarization effect is reduced compared to DRONEs + Light (Figure S9, Supporting Information). This could be due to 2 reasons, (i) the mitochondrial membrane disruption capability of THPs, and (ii) co-localization of DRONEs at the mitochondria and hence enhanced damage on light activation.

The annexin V/FITC apoptosis assay suggests DRONEs + Light induce greater necrosis compared to apoptosis (Figure S10, Supporting Information).

We then studied the potential of DRONEs to induce ICD when exposed to light. Calreticulin exposure and high-mobility group box 1 (HMGB1) release from tumour cells into the extracellular matrix were measured after treatment with different groups. U87 cells treated with DRONEs + Light released 3385 ± 469.45 pg/ml of HMGB1, which is ~6 fold greater than that of the control (Figure 3f). Similarly, cells treated DRONEs + Light showed strong green fluorescence which is indicative of "eat-me" signals expressed on the cell surface (Figure 3g).

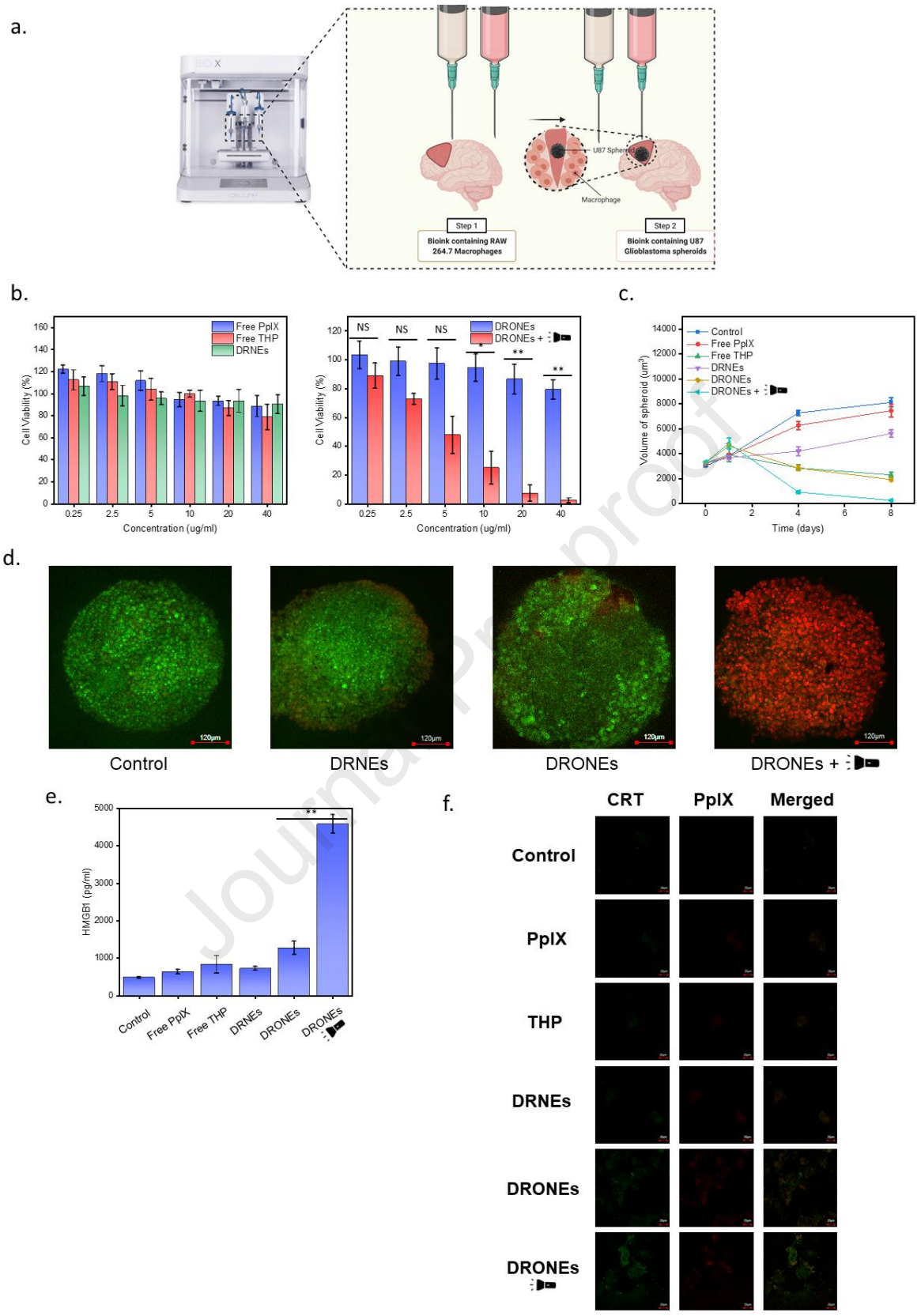

Figure 3. In-vitro therapeutic activity of DRONEs in 3D printed mini-brains. a) Schematic illustration of fabrication of mini-brains, b) Survival rate of U87 spheroids with free PpIX, free THP, DRNEs, and DRONEs with/without irradiation (130 mW cm^{-2}, 5 min) at various concentrations after 24 h of

incubation, c) Reduction in tumour volume as a function of time, d) Confocal images of live/dead viability assays in U-87 spheroids treated with samples (based on IC50) for 6 h (Scale bar: 120 µm), e) Quantification of extracellular release of HMGB1 from U87 spheroids after 6 h of incubation with treatment groups (based on IC50), f) Cell surface expression of CRT after treatment with different treatment groups (based on IC50) for 6 h (Scale bar: 20 µm). Levels of significance were set at the probability of *$p < 0.05$, **$p < 0.01$, ***$p < 0.001$. Error bars represent Mean ± SD ($n \geq 3$).

5.4 Organelle specific co-localization and enhanced penetration of DRONEs

The internalization of free PpIX, DRNEs and DRONEs into U87 cells over 3h and 6h were studied using flow cytometry and confocal microscopy. DRONEs were taken up by U87 cells more readily compared to free PpIX and DRNEs (Figure 4 a and b). This was further confirmed using flow cytometry results with a ~ fold increase in the uptake of DRONEs compared to DRNEs at 6 h (Figure 4c and d).

To further study the internalization pathway of DRONEs, U87 cells were pre-treated with endocytic inhibitors, namely dynasore, chlorpromazine, genistein, and wortmannin. The endocytosis of DRONEs is an energy dependent pathway as no red fluorescence can be observed when the U87 cells were pre-incubated at 4ºC before being treated with DRONEs for 6h (Figure S11, Supporting Information). Furthermore, dynasore significantly reduced the uptake of DRONEs, suggesting either clathrin or caveolae mediated endocytosis. Compared to cells pre-treated with genistein, the uptake of DRONEs cells pre-treated with chlorpromazine was significantly reduced. On the other hand, wortmannin had no effect on the uptake of DRONEs into U87 cells, demonstrating that micropinocytosis was not involved in the internalization of BIONs. This suggests that internalization of DRONEs into U87 cells is primarily through clathrin mediated endocytosis.

To confirm the trafficking of DRONEs to the mitochondria of the tumour cell, we stained various organelles such as lysosomes (Lyzotracker green), mitochondria (Mitotracker green), endoplasmic reticulum (ER tracker), golgi apparatus (Golgi tracker) and a macropinosome marker (^{RhoB}dextran, 70 kDa). The affinity of the THP towards the mitochondria drives the transport of DRONEs to the mitochondria (Figure 4e). This results in a relatively high Pearson correlation coefficient (PCC) of 0.84, as the fluorescent signals of DRONEs co-localized with that mitochondria, whereas PCC of 0.18, 0.36, 0.13 and 0.26 were obtained using fluorescent signals of DRONEs co-localized with golgi apparatus, lysosomes, macropinosome and ER, respectively (Figure 4f).

We then studied the tumour penetration ability of DRONEs into solid tumours using U87 spheroids. The fluorescence intensity of PpIX was measured using confocal microscopy to study the extent of penetration of free PpIX, DRNEs, and DRONEs into the spheroids (Figure 4g). These images were then processed using Image J and converted into 3D surface plots (Figure 4h). Spheroids treated with DRONEs had enhanced penetration capability compared to free PpIX and DRNEs, which were primarily restricted to the spheroid boundaries. The penetration into the solid tumour could be either due to paracellular diffusion or transcellular transport through the extracellular matrix. To further elucidate the penetration mechanism, we pre-incubated the spheroids with either chlorpromazine or Exo-1 (Figure 4i). The inhibition of the penetration of DRONEs into the spheroids, suggests that the penetration of DRONEs could be via transcytosis that depends on clathrin mediated endocytosis and exocytosis.

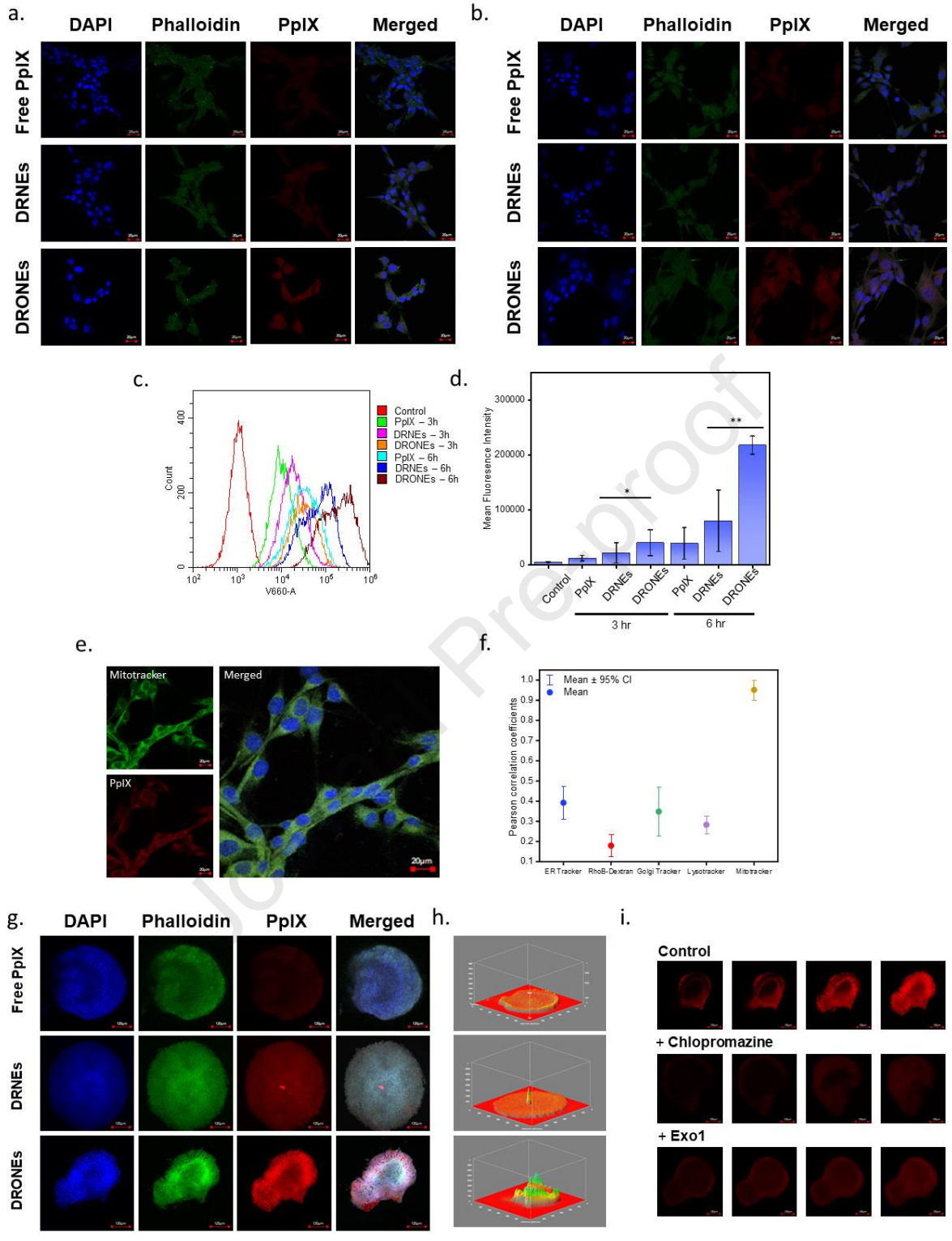

Figure 4. Organelle targeting and tumour penetration of DRONEs. Internalization of free PpIX, DRNEs and DRONEs after a) 3 h and b) 6 h of incubation with U87 cells (Scale bar: 20 µm), c) Flow cytometry analysis and d) Mean Fluorescence Intensity of the internalization of free PpIX, DRNEs and DRONEs after 3 h and 6 h of incubation with U87 cells by measuring the PpIX fluorescence intensity, e) Confocal microscopy observations of co-localization of DRONEs within the mitochondria, f) Pearson correlation coefficients for Golgi tracker, ER tracker, Lysosome tracker, Mitochondria tracker and ^{RhoB}Dextran,

calculated by pixel intensity using Image J, g) Tumour penetration of free PpIX, DRNEs and DRONEs post incubation for 6 h (Scale bar: 120 µm), h) 3D surface plot analysis of confocal images of U87 spheroids treated with different formulations, i) Effects of chlorpromazine and Exo1 on the penetration of BIONs into U87 spheroids (Scale bar: 120 µm). All experiments were run based on PpIX IC50. Levels of significance were set at the probability of *p < 0.05, **p < 0.01, ***p < 0.001. Error/ bars represent Mean ± SD (n ≥ 3).

5.5 DRONEs cross the Blood Brain Barrier and reach the tumour interstitium

DRNEs could hardly be detected outside of the blood vessels labelled with von Willebrand factor in the intracranial tumours at 6 h after intravenous (I.V.) injection, suggesting their inability to cross the blood brain barrier (BBB) and reach the tumour parenchyma (Figure 5b and c). In contrast, DRONEs were readily detected in the tumour parenchyma at 6 h after I.V. injection. This enhanced permeability could be attributed to THP-mediated endocytosis across the BBB [46]. The CGKRK peptide which binds to the p32 protein abundantly present on GBM cells [47], provides the targeting ability that enables preferential accumulation of DRONEs within the tumour [48, 49]. Hence, DRONEs cross the BBB, allowing effective photodynamic therapy and subsequent induction of an immune response in the tumour area.

5.6 Biodistribution and route of elimination of DRONEs

The BBB penetration of DRONEs was studied in an orthotopic mice model (Figure 5a). DRONEs and DRNEs had desirable blood clearance kinetics with ~2-fold increase in blood residence time compared to that of a standard long-circulating PEG–drug conjugate PEG-SS-CPT[50](Figure 5d), which suggests that they remain stealthy and stable in blood circulation. DRONEs did not release PpIX in the mouse plasma (Figure S12, Supporting Information) and no hemolysis was observed after 24 hours of culture (Figure S13, Supporting Information), which proves the excellent stability of DRONEs during blood circulation. Furthermore, DRONEs exhibited relatively slower clearance from blood compared to DRNEs. This could be due to the presence of THP, which enables BBB crossing and tumour homing and penetration, resulting in greater concentration of PpIX in the brain in comparison with blood[48].

The biodistribution of DRONEs was studied on the orthotopic glioblastoma mice model. One week post-intracranial tumour implantation, the mice were intravenously injected with DRONEs via the tail vein, and monitored for 24 h post-injection using IVIS imaging. At 2 h post-injection, DRONEs were broadly distributed throughout the body and a strong PpIX fluorescence signal was detected at the tumour implantation site. At 4 h and 8 h, the PpIX fluorescence signal intensifies at the tumour site. Interestingly, at 24 h, no obvious signal was observed throughout the body except at the tumour site. (Figure 5e). Since epifluorescence imaging can be challenging for both accurate attribution of the fluorescence intensity to precise anatomical spots and distinct signal quantification in whole-body imaging, ex-vivo imaging was performed for excised major organs from all experimental groups (Figure 5f). Quantification of the PpIX distribution profiles indicated that DRONEs had relatively low levels in the lung, spleen and heart. Notably, at 24 h, DRONEs accumulated in the liver, kidney, and tumour. In contrast, DRNEs showed weak PpIX fluorescence signal in all the organs except the kidney, which suggests a rapid renal clearance compared to DRONEs. These results are consistent with previous studies which posits that intravenously administered nanoparticles are predominately eliminated by the mononuclear phagocyte system (MPS), which includes the liver and kidney[51]. The intratumoural PpIX contents at 24 h post-DRONEs injection were 4-fold greater than those of DRNEs (Figure 5g). While performing in-vivo IVIS imaging, due to the anatomical structure of the liver and kidneys deep within the abdominal cavity, strong fluorescence signal could not be detected. These biodistribution

profiles validates the BBB penetration and effective tumour-targeting capabilities of DRONEs with a consistent route of elimination.

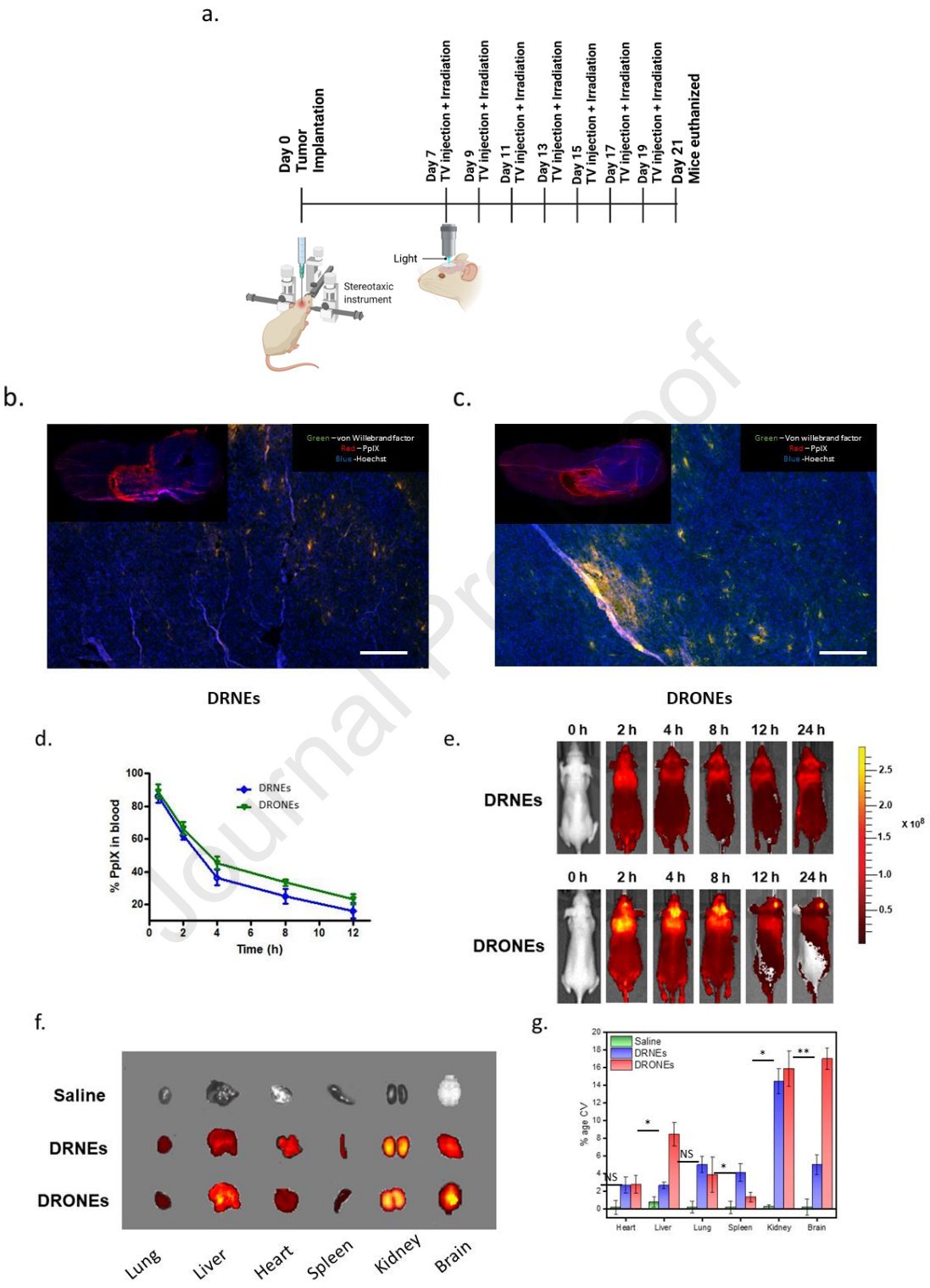

Figure 5. BBB penetration, blood clearance kinetics and biodistribution of DRONEs in U87GM bearing mice. a) Treatment regimen of DRONEs in an orthotopic mice model. TissueFAXs images of b) DRNEs and c) DRONEs distribution on brain tumour sections at high magnification (Scale bar: 100 μm). Blood vessels are immunostained for von Willebrand factor (vWF, green). DRONEs are distributed in the tumour parenchyma compared to DRNEs which are seen only inside the blood vessels, d) Blood clearance kinetics of DRNEs and DRONEs, e) Fluorescence images of mice injected with DRNEs and DRONEs at different time points, f) Fluorescence images of excised organs from mice treated with DRNEs and DRONEs after 24 h, g) The averaged fluorescence intensity within each organ of each group 24 h post-treatment. Levels of significance were set at the probability of *$p < 0.05$, **$p < 0.01$, ***$p < 0.001$. Error bars represent Mean ± SD ($n \geq 3$).

5.7 DRONEs increase survival of U87-glioblastoma bearing mice

In clinics, large tumours are extremely challenging to treat and often lead to poor survival, even in mouse models, large tumours respond poorly to treatment [52]. We challenged DRONEs to the treatment of tumours of ~100 mm^3 as an inoperable model. In an orthotopic glioblastoma mice model, repeated I.V. injections of DRONEs did not cause any acute immune-mediated anaphylaxis-like side effects. The antitumour activity of DRONEs was evaluated in terms of the body weight, tumour volume and survival percentage. The body weights of mice treated with saline, DRNEs and DRONEs reduced significantly during the treatment window (Figure 6a). On the other hand, mice treated with DRONEs + Light, increased in weight till day 12 after which experienced a slight weight reduction. Tumour volumes were determined from U87GM-bearing brains harvested from mice euthanized 14 days post-treatment (Figure 6b). The excised brains from U87GM-bearing mice treated with saline were deformed, hence the tumour volume of the saline group was smaller than that of DRNEs. More importantly, DRONEs + Light showed a significantly higher tumour inhibition activity compared to saline, DRNEs and DRONEs. After alternate day injections of DRONEs and subsequent light irradiation, the tumours almost disappeared after 21 days. Measurement of the tumour volume days after the final treatment showed that DRONEs + Light had a ~100% tumour inhibition, significantly higher than those of saline, DRNEs and DRONEs. Excised brain images suggest that DRONEs + Light can significantly reduce tumour volume and retain the brain structure similar to the healthy brain (Figure 6c). Haematoxylin and eosin staining of brain slices clearly shows the tumour location and its boundary with healthy tissue (Figure 6d).

Next, we assessed the expression of protein markers in the harvested brain tissue and analyzed them using Western Blot to decode the in-vivo apoptotic signaling pathway (Figure 6e). Proteins of interest include BAX, BCL-2 and cleaved caspase-3. DRONEs + Light showed greater expression of BAX proteins compared to the negative control GADPH. THP mediated mitochondrial destabilization and ROS generation by PDT treatment enhanced DNA damage and upregulated BAX expression (Figure 6f). Downregulated Bcl-2 and upregulated BAX expression resulted in the decline of the Bcl-2•BAX heterodimer and boosted the BAX oligomer, Bcl-2, an anti-apoptotic protein that binds to BAX [53]. Through a series of cellular processes, BAX oligomers cleave caspase-3 via the mitochondrial membrane. Changes in the mitochondrial membrane potential ($\Delta\Psi m$) result in the release of cytochrome-C to the cytosol, and subsequent caspase-3 activation which plays a crucial role in apoptosis and cell death. These results validate that DRONEs when exposed to light induce apoptosis in-vivo.

Survival of mice bearing intracranial U87GM and treated with DRNEs or DRONEs with/without light (130 mW/cm^2, 5 min) was investigated over 21 days using the Kaplan-Meier survival analysis. Change in physical appearance such as hunched back posture, exophthalmia, enophthalmia, and loss of body weight was established as endpoints, after which the mice were euthanized (Figure S14,

Supplementary Information). Both DRNEs and DRONEs failed to significantly increase survival compared to saline treatment (Figure 6g), which could be due to their inability to cross the BBB and minimal toxicity without light, respectively. Crucially, DRONEs + Light significantly improved animal survival compared to saline.

No significant differences were observed in the architecture of stained organ sections in the groups treated with saline and DRONEs + Light, indicating that DRONEs + Light did not cause any undesirable side effects (Figure 6h). Interestingly, no nephrotoxicity or hepatotoxicity was observed, even though the liver and kidney were the primary route of elimination of DRONEs. Furthermore, blood chemistry examination of the DRONEs-treated mice showed comparable levels amongst treatment groups (Figure S15, Supporting Information). DRONEs also showed excellent hemocompatibility (Figure S16, Supporting Information). These results affirm the safety and biocompatibility of DRONEs.

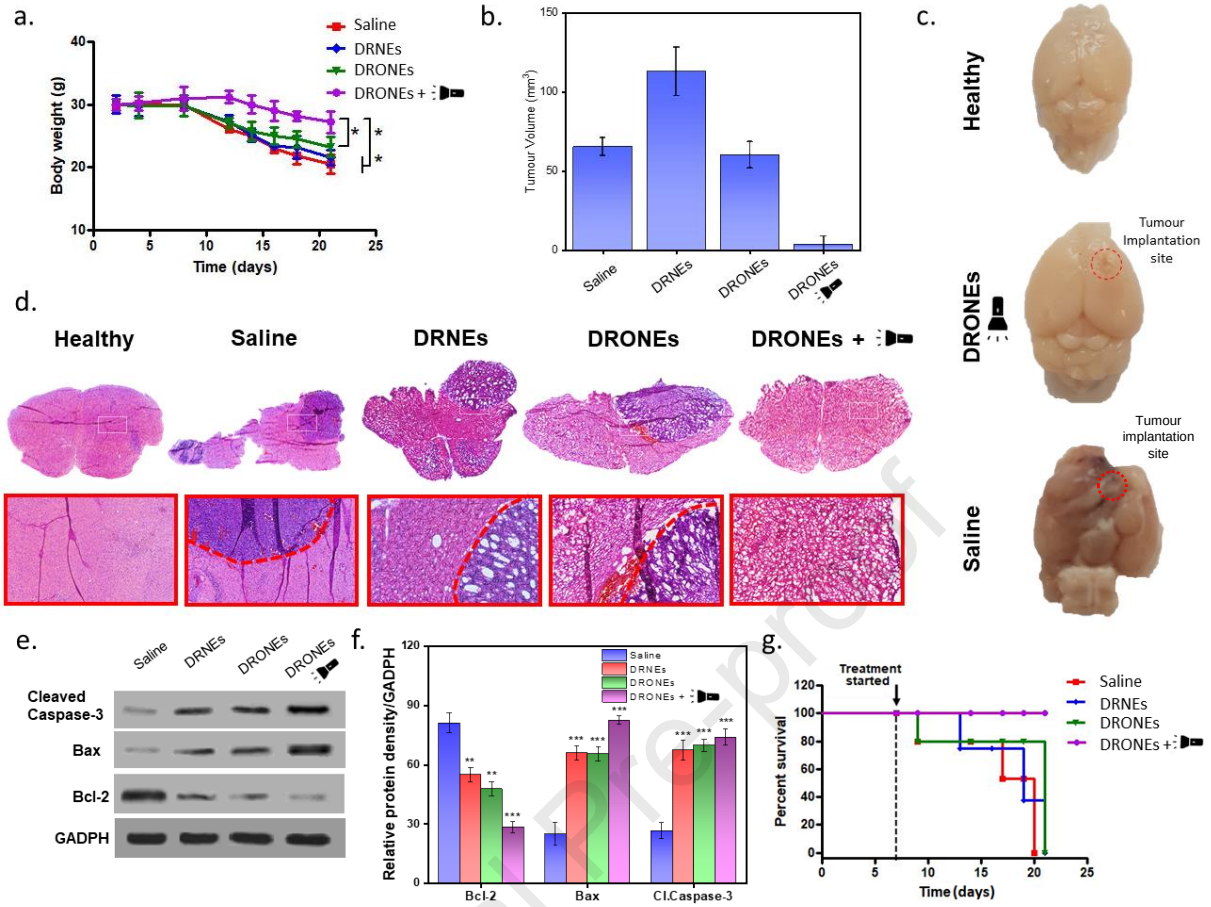

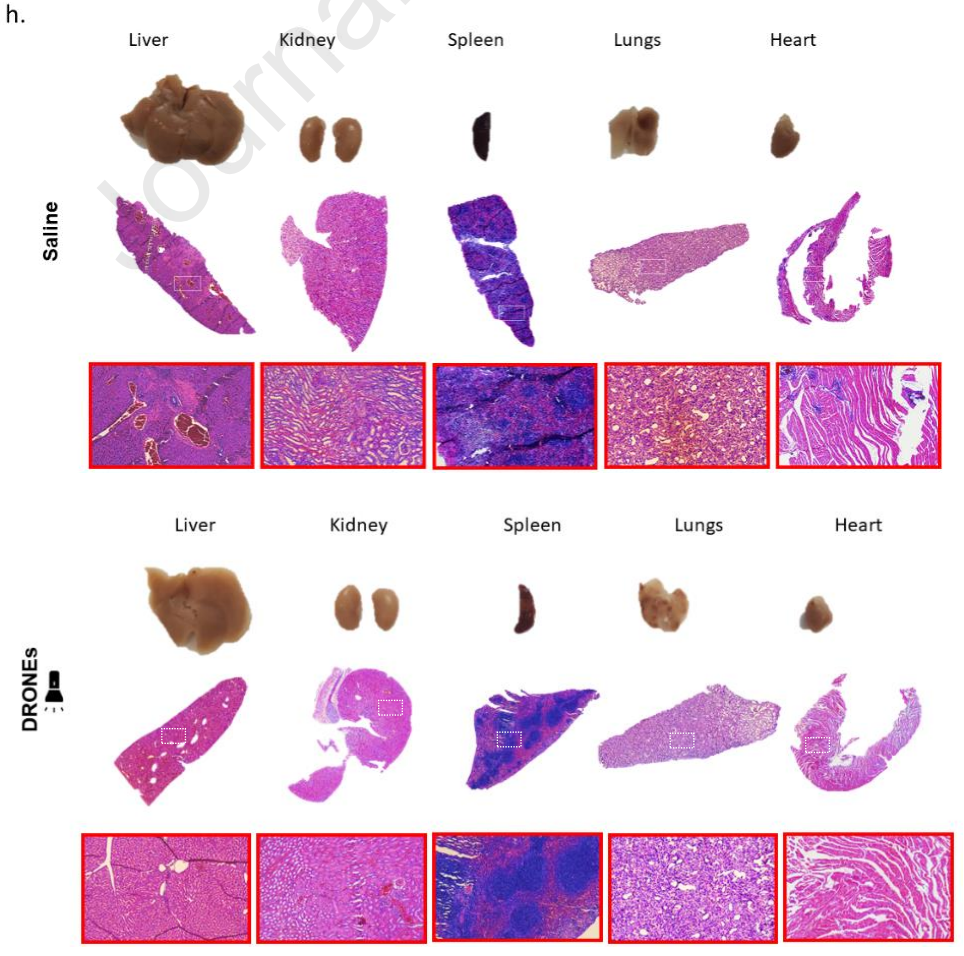

Figure 6. Antitumour activity of DRONEs against orthotopic glioblastoma tumours. a) The body weight variation of tumour-bearing mice during the treatment window, b) Tumour volume 21 days post-treatment, c) Images of excised brains (21 days) of healthy mice and tumour bearing mice treated with DRONEs or saline, d) H&E images of excised brain 21 days post-treatment (Scale bar: 100 µm), e and f) Quantification of cleaved caspase-3, Bax, Bcl-2 using Western blot, g) Kaplan–Meier analysis of the mice, h) Organ and histology section of mice treated with saline or DRONEs + Light (Scale bar: 100 µm). Levels of significance were set at the probability of *$p < 0.05$, **$p < 0.01$, ***$p < 0.001$. Error bars represent Mean ± SD ($n \geq 3$).

5.8 DRONEs stimulate in-situ DC maturation and T-lymphocyte proliferation

We excised the brain from the orthotopic glioblastoma mice model to study the immunostimulative effects of DRONEs and subsequently its ability to function as an in-situ vaccine by triggering an adaptive immune response (Figure 7a). DRONEs when activated with light are capable of inducing ICD and subsequent release of TAAs, which is the first step of eliciting an immune response. In the presence of glioblastoma brain slices (GBSs), the immunostimulative effects of DRONEs were studied by measuring the surface expression of a maturation marker CD83 and a costimulatory molecule CD86 on monocyte derived dendritic cells (Mo-DCs). Immature dendritic cells (iDCs) were considered to be those cells that exhibited low CD83 expression. DRONEs when activated with light increases the surface expression levels of CD83 and CD86 on Mo-DCs (Figure 7b and c).

Furthermore, we measured the secretion levels of IL-1β and IL-10 cytokines by DCs. In the presence of GBSs, the secretion levels of IL-1β and IL-10 cytokines from Mo-DCs increased, consistent with other reports[54] (Figure 7d and e). DRONEs + Light downregulated the secretion of the pro-inhibitory IL-10 cytokine, which can modulate immune function by preventing maturation of macrophage and dendritic cells[55]. In contrast, DRONEs + Light increased the secretion of immunostimulatory IL-1β cytokine, which plays an important role in the activation of APCs, T-cell priming and proliferation [56, 57].

The penultimate step of an effective immune response involves T-cell priming and proliferation within the draining lymph node. We co-cultured stimulated DCs with CellTrace Violet labeled allogeneic peripheral blood lymphocytes (PBLs) to study the subsequent T-lymphocyte proliferation. Free PpIX, and DRNEs had almost no effect on the proliferation of $CD3^+$ T lymphocyte in the presence of treated GBSs. DRONEs + Light showed ~3-fold increase in the proliferation of $CD3^+$ T lymphocyte compared to DRONEs (Figure 7f). This increase can be attributed to the release of TAAs from the tumour cells due to light triggered toxicity (ICD and apoptosis), which enable DC maturation and subsequent priming of $CD3^+$ cells into helper $CD4^+$ (Figure 7g) and cytotoxic $CD8^+$ (Figure 7h) subsets.

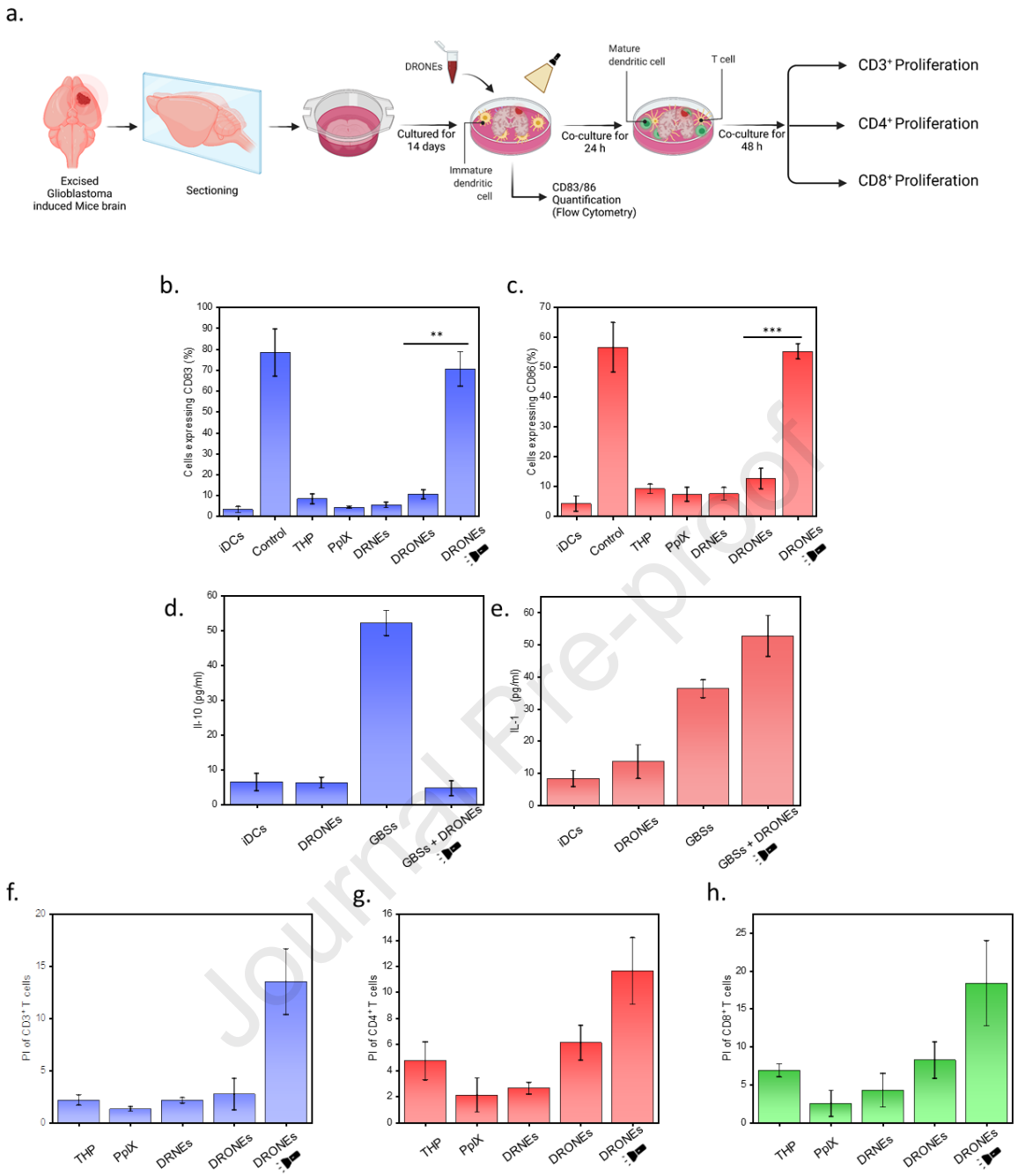

Figure 7. DRONEs modulated in-situ DC maturation and T-lymphocyte proliferation in the presence of organotypic glioblastoma brain slices. a) Schematic illustration of experimental design for evaluating DC maturation and T cell proliferation, Percentage of Mo-DCs expressing b) CD83 and c) CD86 after incubation for 24 h with different treatment groups, Quantification of d) IL-10 and e) IL-1β by stimulated dendritic cells, f) $CD3^+$ T cells, g) $CD3^+$ $CD4^+$ T cells, h) $CD3^+$ $CD8^+$ T cells proliferation response in T-cell-DC co-culture in the presence of GBSs treated with different samples for 24 h. Levels of significance were set at the probability of $*p < 0.05$, $**p < 0.01$, $***p < 0.001$. Error bars represent Mean ± SD ($n \geq 3$).

5.9 Modelling delivery outcomes of DRONEs

The modeling study is performed to compare the delivery outcomes using DRNEs, DRONEs and SRONEs under the delivery conditions with and without GSH. The modeling predicted nanoparticle concentration in tumour tissue is shown in Figure 8a. The concentrations of DRNEs remain low over

time owing to the difficulties in crossing the BBB. Both DRONEs and SRONEs can successfully accumulate in tumour tissue. Moreover, since SRONEs is less sensitive to GSH, the comparable concentrations can be achieved for SRONEs under both the delivery conditions and DRONEs delivered without GSH. Using GSH is effective to accelerate the drug release from DRONEs, and consequently leads to the highest PpIX concentration in tumour tissue, as shown in Figure 8b. Similarly, the delivery using SRONEs results in the comparable PpIX concentrations as DRONEs without GSH. The worst delivery outcomes are found for DRNEs.

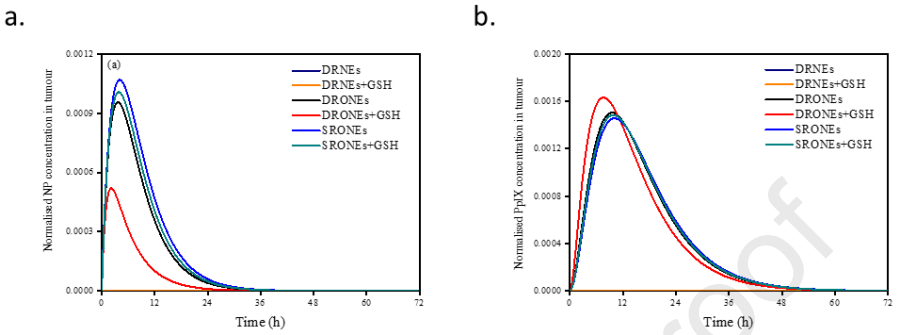

Figure 8. Modeling predicted time course of a) nanoparticle and b) PpIX concentration in tumour. The concentration is normalized by the initial drug concentration in the system plasma.

6. Conclusion

In conclusion, to overcome the hurdles in the clinical translation of nanomedicine, we developed dual responsive organelle targeted nanoreactors (DRONEs). Site specific payload release can be realized using DRONEs as it leverages of redox and pH stimuli to release the intact photosensitizer and tumour homing pro-apoptotic peptide in a backbone-shattering manner. Notably, DRONEs show excellent BBB penetrating and tumour homing potential in an orthotopic glioblastoma mice model which enable effective tumour burden reduction with no apparent toxicity to other vital organs. Furthermore, DRONEs show superior biocompatibility and safety along with a reliable route of elimination. Furthermore, as a proof of concept of DRONEs as an in-situ vaccine, they are capable of triggering an adaptive immune responsive, with DC maturation and subsequent T-lymphocyte proliferation, thereby enabling antitumoural immunity. However, it is necessary to prove its potential to achieve anti-tumoural immunity in an in-vivo tumour rechallenge model. The modeling results demonstrate the importance and effectiveness of tumour homing and dual trigger in improving the drug delivery outcomes. As an extension of its current application, we envisage DRONEs can be used as a contrast agent to directly track therapeutics embedded in its backbone via fluorescence imaging. Furthermore, it is critical to develop non-invasive or minimally invasive optical fibers or delivery devices which can enable optimal light exposure to the target tissue. Its precise composition, site specific payload release and direct drug tracking make DRONEs strong candidates as the next generation of personalized cancer treatments in the clinic.

7. Experimental Section

Materials: A complete list of materials, reagents and equipment used in this study can be found in the Supporting Information.

Preparation of DRP: Protoporphyrin IX (100 mg, 0.177 mmol), EDC (73 mg, 0.3806 mmol) and NHS (44 mg, 0.3806 mmol) were dissolved in 28 ml of DMSO and stirred in the dark for 12 h at room

temperature. Cystamine dihydrochloride (38.115 mg, 0.169 mmol) dissolved in 2 ml DMF was then added to the above mixture and stirred for 24 h. Meanwhile, NH2-PEG-MAL (MW – 2 KDa) (71 mg, 0.0355 mmol) and THP (78.26 mg, 0.0373 mmol) were dissolved the 10 ml DMSO and stirred for 24 h in the dark at room temperature. The resulting mixtures were then stirred together for 24 h in the dark. The resulting solution was dialyzed for 24 h using an 8000 MWCO dialysis bag and lyophilized to obtain DRP. DRP without THP was prepared in a slightly modified method where NH2-PEG-MAL and THP are replaced with the addition of NH2-PEG-COOH at the same step.

Preparation of DRNEs, SRONEs and DRONEs: DRNEs and DRONEs were prepared by nanoprecipitation. DRP was dissolved in THF and added to 1x PBS drop by drop. The solution was stirred overnight to allow solvent evaporation. Similarly, DRP without THP was used to prepare DRNEs. SRONEs were fabricated via the same process by replacing cystamine dihydrochloride in the backbone with ethylene diamine (EDA).

Characterization of DRONEs: Detailed characterization of DRONEs is explained in the Supporting Information.

In Vitro Release Studies: Dual responsive backbone shattering payload release experiments performed by placing 400µl of DRONEs and SRONEs into an MWCO 2K Slide-A-Lyzer MINI dialysis device with a 2000 molecular weight cut-off (ThermoFisher Scientific, USA). The samples were dialyzed against 1.4 ml of releasing media, pH 7.4 PBS, and pH 5.0 sodium acetate buffer with/without GSH (10 mM) and incubated at 37°C on a platform shaker at 150 r.p.m. At predetermined intervals (1, 2, 4, 8, 12, 24 h), the medium was withdrawn (100µl) for analysis and replaced with the same amount of fresh medium to maintain the final volume constant during the release experiment.

Glioblastoma organotypic Brain Slices: The excised tumour induced mice brain was sliced into 350 µm slices using a Mcllwain tissue chopper and laid down on a transwell insert, placed in 6 well plates containing α-MEM media and cultured for 14 days at 37°C in a 5% CO2 incubator.

3D Bio-printing Mini-brains: The prepared bioink was warmed 37°C and added to cells, followed by repeated mixing to ensure a homogenous solution. A cell density of 3 x 106 RAW 264.7 macrophages/ml and U87 spheroids (2000 cells/ml) was used for all experiments. The bioink containing cells was transferred into a sterile syringe (Terumo) equipped with a 30G blunt needle (Cellink) and allowed to gelate for 15 min at room temperature. Cell laden mini-brains were bioprinted onto a sterile microscope slide via pressure-based extrusion and immediately crosslinked by exposure to UV light (λ 365nm, 12 mW/cm2) for 2 min. The bioprinted mini-brains were washed with DPBS thrice and in complete DMEM medium before being transferred to the incubator and cultured for 4 days.

Therapeutic efficacy of DRONEs on 3D printed mini brains: The cytotoxicity of free PpIX, free THP, DRNEs and DRONEs (PpIX concentration range 0.25-40 µg/ml) was evaluated on 3D U87 spheroids sectioned from the mini-brains with/without light (130 mW/cm2, 5 min). Free PpIX, free THP, and DRNEs were tested in concentrations correspondent to the amounts in DRONEs. Cell viability of the spheroids was measured using CellTiter-Glo 3D Cell Viability Assay (Promega Corp., USA) after 24 h of incubation. Live/Dead Viability/Cytotoxicity Kit (ThermoFisher, USA) was used to visualize the therapeutic efficacy of free drugs, DRNEs and DRONEs with/without light. Briefly, spheroids were incubated with DRONEs (PpIX 4 µg/ml) (130 mW/cm2, 5 min). Similarly, free PpIX, free THP, and DRNEs were tested in concentrations similar to DRONEs. Images were acquired using confocal microscopy (FV1000, Olympus Corp., Japan).

DCFH-DA was used to evaluate the potential of DRONEs to generate ROS when exposed to light. DRONEs (PpIX 4 µg/ml) were incubated with U87 cells for 6 h and irradiated with light (130 mW/cm2, 5 min). Free THP, free PpIX, and DRNEs were also tested for their ROS generating capability at corresponding concentrations. Furthermore, the resulting mitochondrial membrane damage from

ROS generation was assessed using JC-1 assay (ThermoFisher Scientific, USA). Manufacturer's instructions were followed for both the experiments before image acquisition using confocal microscopy.

Annexin V-FITC/PI Apoptosis Detection Kit (ThermoFisher Scientific, USA) was used to study the extent of apoptosis in the treated spheroids. Manufacturer's protocol was followed before Annexin V-FITC apoptosis detection using flow cytometry (Cytoflex, Beckman Coulter).

The induction of ICD was studied by measuring the HMGB1 release and calreticulin exposure. U87 cells were treated with various treatment groups with/without light irradiation (130 mW/cm2, 5 min) at equivalent concentrations for 6 h. The cells were first fixed using 4% formaldehyde, followed by permeabilization using 0.1 % Triton-X, and blocking using 1% gelatin. Subsequently, the cells were incubated with an anti-calreticulin antibody for 1 h at RT, followed by incubation with Alexa Fluor 488-conjugated secondary antibody for 1 h at RT. The images were obtained using confocal microscopy. The cells were washed with DPBS three times at each step.

Human HMGB1 Elisa Kit (Novus Biologicals) was used to measure the Extracellular HMGB1 released into the serum-free media from the spheroids treated with different groups.

Cellular Uptake of DRONEs: The internalization rates of free PpIX, DRNEs, and DRONEs (PpIX concentration 4 µg/ml) for 3 h and 6 h were assessed using confocal microscopy. After incubation, the cells were fixed using 300 µl of 4% paraformaldehyde for 20 min, stained with 300µl of Phalloidin-IFluor-488 (Abcam, UK) for 45 min and 300 µl of DAPI (ThermoFisher Scientific, USA) for 5 min. The cells were washed thrice with DPBS at each step. For flow cytometry, the treated cells were trypsinized, washed with cold PBS thrice, and immediately analyzed.

Endocytic pathway of DRONEs: To study the endocytic pathway of DRONEs, four endocytosis inhibitors were used (dynasore, wortmannin, genistein, chlorpromazine). U87 cells were pre-incubated with these inhibitors at concentrations of 50 µM, 25 µM, 100 µM, and 50 µM respectively for 1h. The cells were then treated with DRONEs for 6 h. The cells were fixed and analysed using confocal microscopy. The cells were washed with DPBS three times at each step.

Intracellular trafficking of DRONEs in U87 cells: The U87 cells were treated with DRONEs for 6 h, then the lysosomes were stained with LysoTracker Green (50 nM) for 45 min, the mitochondria was stained using Mitotracker Green (20 nM), the macropinosomes were labeled by 70 kDa ^{RhoB}dextran (250 µg/ml) for 45 min, Golgi and Endoplasmic Reticulum were marked with Golgi Staining Kit Green and ER Staining Kit Green respectively, according to the manufacturer's instructions. A confocal laser scanning microscope was used to capture the images.

Penetration of DRONEs in 3D spheroids: Spheroids sectioned from mini-brains were treated with free PpIX, DRNEs and DRONEs similar to the cell uptake study for 6 h. The spheroids were fixed with 100 µl of 4% paraformaldehyde for 20 min, permeabilized using 100 µl of 0.1 % Triton-X for 10 min, dehydrated, and rehydrated using cold methanol (0, 25, 50, 75, 100 %) for 10 min each. The spheroids were incubated with 10 µl of CytoVista 3D cell culture clearing reagent (ThermoFisher Scientific, USA) before imaging using confocal microscopy.

Biodistribution of DRONEs in glioblastoma bearing mice model: The orthotopic glioblastoma bearing mice were divided into two groups (n = 3) and intravenously (i.v) administered via tail vein with saline (Control group), DRNEs and DRONEs. The mice were then exposed to IVIS Spectrum In Vivo Imaging System (PerkinElmer) for real-time fluorescence imaging at 0, 2, 4, 8, 12, and 24 h after NP injections. At 24 h post-injection the mice were euthanized, and vital organs (heart, liver, lung, spleen, kidneys, and brain) were collected for ex-vivo fluorescence imaging.

Antitumour efficacy in U87MG bearing mice: The in-vivo anti-glioblastoma efficacy of DRONEs was evaluated in an orthotopic brain tumour mice model. The orthotopic U87MG glioblastoma-bearing

mice were randomly divided into four groups (n = 5) and treated with the following treatment regimens by tail intravenous administration: (i) 200 µL of saline, (ii) DRNEs (5 mg/kg to body weight), (iii) DRONEs without light irradiation (5 mg/kg to body weight) and (iv) DRONEs with light irradiation (5 mg/kg to body weight) on day 7 post U87MG cell implantation. After 8 h post i.v injection, the mice were irradiated with 630 nm (130 mW/cm2, 5 min) light at the tumour sites. The treatment regimens involved injection through the tail vein three days a week for 2 weeks. The mice (control group) with U87MG glioblastoma were untreated and groups treated with DRNEs did not receive irradiation. The animals' general health, weight, and grooming were monitored daily. The survival time was documented and evaluated from day 0 ever since tumour implantation to the day of demise. Kaplan-Meier survival method using Graphpad Prism software was used to plot the survival curve for all four groups.

At day 21, three mice of each group were sacrificed by transcardial perfusion with 10 mL PBS and 4% paraformaldehyde to clear the residual NPs from the blood vessels. The brains were harvested and fixed in PBS with 30% sucrose (cryoprotection) for 5-7 days and frozen swiftly in Tissue Tek O.C.T compound on dry ice. Using a cryostat microtome (Leica), the brain was sectioned into 20 µm (stored at -20 °C until use) and processed for hematoxylin and eosin (H&E) staining, and then visualized under a TissueFAXS Scanner.

BBB penetration efficiency of DRONEs was studied using immunofluorescence staining. The sectioned brain slices were rehydrated with wash buffer and then subjected to antigen retrieval using a hot water bath at 90 °C for 3-5 min. The samples were then blocked with 3% H2O2 in water for 5 min before incubation with primary (sheep polyclonal to Von Willebrand Factor) and secondary antibody (Donkey Anti-sheep IgG H&L Alexa Fluor 488), followed by nucleus counterstained with Hoechst. The brain sections were then imaged using a TissueFAXS Scanner.

Blood clearance kinetics of DRNEs and DRONEs: Mice used in the in-vivo antitumour efficacy study was used for this experiment. The orthotopic glioblastomas bearing mice were divided into two groups (n = 5) and tail intravenously (i.v) administered with DRNEs and DRONEs. Due to limited blood volume in each animal, we were unable to do multiple blood collection within 24 h from single mice. Hence, we collected blood from five different mice from same group at five different time point (0.5, 2, 4, 8 and 12 h). Blood samples (50 µL) were collected through the tail vein at desired time point and then mixed with 50 µL of NaOH (0.1 N) to extract PpIX. Next, acetonitrile (1 mL) was added, vortexed and centrifuged at 5000 rpm for 5 min. Followed by, 200µl of supernatant was withdrawn and mixed with 200µl of aqueous HCl (0.1N) solution for HPLC analysis. The PpIX content was determined according to the standard curve.

Western Blotting for protein quantification: The harvested brain tumour tissues were washed with PBS thrice and rapidly frozen in liquid nitrogen to quantify the protein expression levels with/without treatment. Briefly, using mortar and pestle the brain tumour tissues were grounded and homogenised in RIPA buffer containing a protease/phosphatase inhibitor cocktail. Tumour lysis was centrifuged for 20 min at 12,000 rpm (4 °C), and the protein concentration in the supernatant was measured by BCA Protein Assay Kit. Protein samples were mixed with 4× Laemlli loading buffer containing β-mercaptoethanol and loaded into polyacrylamide gels. Based on their molecular weight, the loaded protein were resolved by SDS-PAGE and transferred onto PVDF membranes. The membranes were washed three times with 1×TBS (Tris-glycine buffer) in methanol and blocked with blocking buffer for an hour at room temperature, followed by incubation with the primary antibodies against Bcl-2, Bax, Cleaved caspase 3, and GADPH (as a loading control). Membranes were then washed in Tween-TBS (TBST) and incubated for 1 h with horseradish peroxidase-conjugated secondary antibodies. Membranes were rinsed thoroughly with TBST before incubating with enhanced chemiluminescence (ECL) detection reagent and the protein bands were imaged using gel-imaging system (G:BOX Chemi XX6, Syngene, USA).

8. Credit Author Statement

Vishnu Sunil: Conceptualization, Methodology, Investigation, Data Curation, Writing – Original Draft. Anbu Mozhi: Conceptualization, Methodology, Investigation, Data Curation. Wenbo Zhan: Methodology, Formal Analysis, Investigation. Jia Heng Teoh: Methodology, Investigation (3D printing). Chi-Hwa Wang – Conceptualization, Supervision, Writing – Review and Editing, Funding Acquisition.

9. Declaration of Competing Interests

The authors declare that they have no known competing financial interests or personal relationships that could have appeared to influence the work reported in this paper.

10. Acknowledgement

This project is supported by the Economic Development Board Singapore and National University of Singapore under the grant N279-000-030-001. The project received partial support in the following grants: NAMIC Singapore and funded by the National Research Foundation Singapore under its Innovation Cluster Programme under the project number, 2018239 and grant number, R-279-000-577-592. Singapore National Research Foundation, Grant No.: R-719-000-018-281. The authors would like to thank Mr. Lim You Kang for all his technical assistance in this project. Vishnu Sunil and Jia Heng Teoh greatly appreciate the National University of Singapore Research Scholarship for the funding of their Ph.D. studies at the National University of Singapore.

11. Data Availability statement

The raw/processed data required to reproduce these findings cannot be shared at this time as the data also forms part of an ongoing study.

12. References

[1] V. Sunil, A. Mozhi, W. Zhan, J.H. Teoh, C.-H. Wang, Convection enhanced delivery of light responsive antigen capturing oxygen generators for chemo-phototherapy triggered adaptive immunity, Biomaterials (2021) 120974.
[2] G. Mikhaylov, U. Mikac, A.A. Magaeva, V.I. Itin, E.P. Naiden, I. Psakhye, L. Babes, T. Reinheckel, C. Peters, R. Zeiser, Ferri-liposomes as an MRI-visible drug-delivery system for targeting tumours and their microenvironment, Nature nanotechnology 6(9) (2011) 594-602.
[3] S. Mignani, J. Rodrigues, H. Tomas, M. Zablocka, X. Shi, A.-M. Caminade, J.-P. Majoral, Dendrimers in combination with natural products and analogues as anti-cancer agents, Chemical Society Reviews 47(2) (2018) 514-532.
[4] P. Davoodi, L.Y. Lee, Q. Xu, V. Sunil, Y. Sun, S. Soh, C.-H. Wang, Drug delivery systems for programmed and on-demand release, Advanced drug delivery reviews 132 (2018) 104-138.
[5] A.C. Anselmo, S. Mitragotri, Nanoparticles in the clinic: An update, Bioengineering & translational medicine 4(3) (2019) e10143.
[6] V. Bhardwaj, A. Kaushik, Z.M. Khatib, M. Nair, A.J. McGoron, Recalcitrant issues and new frontiers in nano-pharmacology, Frontiers in pharmacology 10 (2019) 1369.
[7] A. Mozhi, V. Sunil, W. Zhan, P.B. Ghode, N.V. Thakor, C.-H. Wang, Enhanced penetration of pro-apoptotic and anti-angiogenic micellar nanoprobe in 3D multicellular spheroids for chemophototherapy, Journal of Controlled Release 323 (2020) 502-518.
[8] J. Li, Y. Li, Y. Wang, W. Ke, W. Chen, W. Wang, Z. Ge, Polymer prodrug-based nanoreactors activated by tumor acidity for orchestrated oxidation/chemotherapy, Nano letters 17(11) (2017) 6983-6990.
[9] X. Hu, G. Liu, Y. Li, X. Wang, S. Liu, Cell-penetrating hyperbranched polyprodrug amphiphiles for synergistic reductive milieu-triggered drug release and enhanced magnetic resonance signals, Journal of the American Chemical Society 137(1) (2015) 362-368.
[10] W. Ha, X.-b. Zhao, X.-y. Chen, K. Jiang, Y.-p. Shi, Prodrug-based cascade self-assembly strategy for precisely controlled combination drug therapy, ACS applied materials & interfaces 10(25) (2018) 21149-21159.
[11] Y. Cong, H. Xiao, H. Xiong, Z. Wang, J. Ding, C. Li, X. Chen, X.J. Liang, D. Zhou, Y. Huang, Dual drug backboned shattering polymeric theranostic nanomedicine for synergistic eradication of patient-derived lung cancer, Advanced Materials 30(11) (2018) 1706220.
[12] P. Zhang, J. Wang, H. Chen, L. Zhao, B. Chen, C. Chu, H. Liu, Z. Qin, J. Liu, Y. Tan, Tumor microenvironment-responsive ultrasmall nanodrug generators with enhanced tumor delivery and penetration, Journal of the American Chemical Society 140(44) (2018) 14980-14989.
[13] J. Rautio, N.A. Meanwell, L. Di, M.J. Hageman, The expanding role of prodrugs in contemporary drug design and development, Nature Reviews Drug Discovery 17(8) (2018) 559-587.
[14] J. Bhattacharyya, J.J. Bellucci, I. Weitzhandler, J.R. McDaniel, I. Spasojevic, X. Li, C.-C. Lin, J.-T.A. Chi, A. Chilkoti, A paclitaxel-loaded recombinant polypeptide nanoparticle outperforms Abraxane in multiple murine cancer models, Nature communications 6(1) (2015) 1-12.
[15] T.-M. Sun, Y.-C. Wang, F. Wang, J.-Z. Du, C.-Q. Mao, C.-Y. Sun, R.-Z. Tang, Y. Liu, J. Zhu, Y.-H. Zhu, Cancer stem cell therapy using doxorubicin conjugated to gold nanoparticles via hydrazone bonds, Biomaterials 35(2) (2014) 836-845.
[16] P. Pei, C. Sun, W. Tao, J. Li, X. Yang, J. Wang, ROS-sensitive thioketal-linked polyphosphoester-doxorubicin conjugate for precise phototriggered locoregional chemotherapy, Biomaterials 188 (2019) 74-82.
[17] B. Sun, C. Luo, H. Yu, X. Zhang, Q. Chen, W. Yang, M. Wang, Q. Kan, H. Zhang, Y. Wang, Disulfide bond-driven oxidation-and reduction-responsive prodrug nanoassemblies for cancer therapy, Nano letters 18(6) (2018) 3643-3650.
[18] W. Wang, Y. Jin, X. Liu, F. Chen, X. Zheng, T. Liu, Y. Yang, H. Yu, Endogenous Stimuli-Activatable Nanomedicine for Immune Theranostics for Cancer, Advanced Functional Materials (2021) 2100386.

[19] S. Han, A. Samanta, X. Xie, L. Huang, J. Peng, S.J. Park, D.B.L. Teh, Y. Choi, Y.T. Chang, A.H. All, Gold and hairpin DNA functionalization of upconversion nanocrystals for imaging and in vivo drug delivery, Advanced Materials 29(18) (2017) 1700244.
[20] G. Song, L. Cheng, Y. Chao, K. Yang, Z. Liu, Emerging nanotechnology and advanced materials for cancer radiation therapy, Advanced Materials 29(32) (2017) 1700996.
[21] G. Tian, X. Zhang, Z. Gu, Y. Zhao, Recent advances in upconversion nanoparticles-based multifunctional nanocomposites for combined cancer therapy, Advanced Materials 27(47) (2015) 7692-7712.
[22] H.-J. Li, J.-Z. Du, J. Liu, X.-J. Du, S. Shen, Y.-H. Zhu, X. Wang, X. Ye, S. Nie, J. Wang, Smart superstructures with ultrahigh pH-sensitivity for targeting acidic tumor microenvironment: instantaneous size switching and improved tumor penetration, ACS nano 10(7) (2016) 6753-6761.
[23] W. Sun, S. Li, B. Häupler, J. Liu, S. Jin, W. Steffen, U.S. Schubert, H.J. Butt, X.J. Liang, S. Wu, An amphiphilic ruthenium polymetallodrug for combined photodynamic therapy and photochemotherapy in vivo, Advanced Materials 29(6) (2017) 1603702.
[24] H.-J. Li, J.-Z. Du, X.-J. Du, C.-F. Xu, C.-Y. Sun, H.-X. Wang, Z.-T. Cao, X.-Z. Yang, Y.-H. Zhu, S. Nie, Stimuli-responsive clustered nanoparticles for improved tumor penetration and therapeutic efficacy, Proceedings of the National Academy of Sciences 113(15) (2016) 4164-4169.
[25] M. Wang, S. Sun, C.I. Neufeld, B. Perez-Ramirez, Q. Xu, Reactive oxygen species-responsive protein modification and its intracellular delivery for targeted cancer therapy, Angewandte Chemie 126(49) (2014) 13662-13666.
[26] D. Luo, K.A. Carter, D. Miranda, J.F. Lovell, Chemophototherapy: an emerging treatment option for solid tumors, Advanced Science 4(1) (2017) 1600106.
[27] K.A. Carter, S. Shao, M.I. Hoopes, D. Luo, B. Ahsan, V.M. Grigoryants, W. Song, H. Huang, G. Zhang, R.K. Pandey, Porphyrin–phospholipid liposomes permeabilized by near-infrared light, Nature communications 5(1) (2014) 1-11.
[28] G. Yu, S. Yu, M.L. Saha, J. Zhou, T.R. Cook, B.C. Yung, J. Chen, Z. Mao, F. Zhang, Z. Zhou, A discrete organoplatinum (II) metallacage as a multimodality theranostic platform for cancer photochemotherapy, Nature communications 9(1) (2018) 1-18.
[29] C. Holohan, S. Van Schaeybroeck, D.B. Longley, P.G. Johnston, Cancer drug resistance: an evolving paradigm, Nature Reviews Cancer 13(10) (2013) 714-726.
[30] P. Wijermans, W. Gerrits, H. Haak, Severe immunodeficiency in patients treated with fludarabine monophosphate, European journal of haematology 50(5) (1993) 292-296.
[31] J.N. Barreto, K.B. McCullough, L.L. Ice, J.A. Smith, Antineoplastic agents and the associated myelosuppressive effects: a review, Journal of pharmacy practice 27(5) (2014) 440-446.
[32] D.W. Hoskin, A. Ramamoorthy, Studies on anticancer activities of antimicrobial peptides, Biochimica et Biophysica Acta (BBA)-Biomembranes 1778(2) (2008) 357-375.
[33] J.C. Mai, Z. Mi, S.-H. Kim, B. Ng, P.D. Robbins, A proapoptotic peptide for the treatment of solid tumors, Cancer research 61(21) (2001) 7709-7712.
[34] F. Araste, K. Abnous, M. Hashemi, S.M. Taghdisi, M. Ramezani, M. Alibolandi, Peptide-based targeted therapeutics: Focus on cancer treatment, Journal of controlled release 292 (2018) 141-162.
[35] G. Perry, A.K. Raina, A. Nunomura, T. Wataya, L.M. Sayre, M.A. Smith, How important is oxidative damage? Lessons from Alzheimer's disease, Free radical biology & medicine 28(5) (2000) 831-834.
[36] H. Pelicano, D. Carney, P. Huang, ROS stress in cancer cells and therapeutic implications, Drug resistance updates 7(2) (2004) 97-110.
[37] P.W. Kantoff, C.S. Higano, N.D. Shore, E.R. Berger, E.J. Small, D.F. Penson, C.H. Redfern, A.C. Ferrari, R. Dreicer, R.B. Sims, Sipuleucel-T immunotherapy for castration-resistant prostate cancer, New England Journal of Medicine 363(5) (2010) 411-422.
[38] I. Melero, G. Gaudernack, W. Gerritsen, C. Huber, G. Parmiani, S. Scholl, N. Thatcher, J. Wagstaff, C. Zielinski, I. Faulkner, Therapeutic vaccines for cancer: an overview of clinical trials, Nature reviews Clinical oncology 11(9) (2014) 509-524.

[39] L. Zitvogel, O. Kepp, G. Kroemer, Immune parameters affecting the efficacy of chemotherapeutic regimens, Nature reviews Clinical oncology 8(3) (2011) 151-160.
[40] C.J. Melief, T. van Hall, R. Arens, F. Ossendorp, S.H. van der Burg, Therapeutic cancer vaccines, The Journal of clinical investigation 125(9) (2015) 3401-3412.
[41] F. Martins, L. Sofiya, G.P. Sykiotis, F. Lamine, M. Maillard, M. Fraga, K. Shabafrouz, C. Ribi, A. Cairoli, Y. Guex-Crosier, Adverse effects of immune-checkpoint inhibitors: epidemiology, management and surveillance, Nature reviews Clinical oncology 16(9) (2019) 563-580.
[42] U. Sahin, Ö. Türeci, Personalized vaccines for cancer immunotherapy, Science 359(6382) (2018) 1355-1360.
[43] H. Wang, D.J. Mooney, Biomaterial-assisted targeted modulation of immune cells in cancer treatment, Nature materials 17(9) (2018) 761-772.
[44] M.G. Vander Heiden, L.C. Cantley, C.B. Thompson, Understanding the Warburg effect: the metabolic requirements of cell proliferation, science 324(5930) (2009) 1029-1033.
[45] V. Sunil, J.H. Teoh, B.C. Mohan, A. Mozhi, C.-H. Wang, Bioengineered immunomodulatory organelle targeted nanozymes for photodynamic immunometabolic therapy, Journal of Controlled Release 350 (2022) 215-227.
[46] L. Lv, X. Li, W. Qian, S. Li, Y. Jiang, Y. Xiong, J. Xu, W. Lv, X. Liu, Y. Chen, Enhanced anti-glioma efficacy by borneol combined with CGKRK-modified paclitaxel self-assembled redox-sensitive nanoparticles, Frontiers in pharmacology 11 (2020) 558.
[47] L. Agemy, V.R. Kotamraju, D. Friedmann-Morvinski, S. Sharma, K.N. Sugahara, E. Ruoslahti, Proapoptotic peptide-mediated cancer therapy targeted to cell surface p32, Molecular Therapy 21(12) (2013) 2195-2204.
[48] L. Agemy, D. Friedmann-Morvinski, V.R. Kotamraju, L. Roth, K.N. Sugahara, O.M. Girard, R.F. Mattrey, I.M. Verma, E. Ruoslahti, Targeted nanoparticle enhanced proapoptotic peptide as potential therapy for glioblastoma, Proceedings of the National Academy of Sciences 108(42) (2011) 17450-17455.
[49] J.A. Hoffman, E. Giraudo, M. Singh, L. Zhang, M. Inoue, K. Porkka, D. Hanahan, E. Ruoslahti, Progressive vascular changes in a transgenic mouse model of squamous cell carcinoma, Cancer cell 4(5) (2003) 383-391.
[50] X.-Q. Li, H.-Y. Wen, H.-Q. Dong, W.-M. Xue, G.M. Pauletti, X.-J. Cai, W.-J. Xia, D. Shi, Y.-Y. Li, Self-assembling nanomicelles of a novel camptothecin prodrug engineered with a redox-responsive release mechanism, Chemical Communications 47(30) (2011) 8647-8649.
[51] S.-D. Li, L. Huang, Pharmacokinetics and biodistribution of nanoparticles, Molecular pharmaceutics 5(4) (2008) 496-504.
[52] A. Wushou, X.C. Miao, Tumor size predicts prognosis of head and neck synovial cell sarcoma, Oncology Letters 9(1) (2015) 381-386.
[53] T.P. Garner, D.E. Reyna, A. Priyadarshi, H.-C. Chen, S. Li, Y. Wu, Y.T. Ganesan, V.N. Malashkevich, E.H. Cheng, E. Gavathiotis, An autoinhibited dimeric form of BAX regulates the BAX activation pathway, Molecular cell 63(3) (2016) 485-497.
[54] O. Bloch, C.A. Crane, R. Kaur, M. Safaee, M.J. Rutkowski, A.T. Parsa, Gliomas promote immunosuppression through induction of B7-H1 expression in tumor-associated macrophages, Clinical cancer research 19(12) (2013) 3165-3175.
[55] S.S. Iyer, G. Cheng, Role of interleukin 10 transcriptional regulation in inflammation and autoimmune disease, Critical Reviews™ in Immunology 32(1) (2012).
[56] E. Voronov, S. Dotan, Y. Krelin, X. Song, M. Elkabets, Y. Carmi, P. Rider, I. Cohen, M. Romzova, I. Kaplanov, Unique versus redundant functions of IL-1α and IL-1β in the tumor microenvironment, Frontiers in immunology 4 (2013) 177.
[57] S.Z. Ben-Sasson, J. Hu-Li, J. Quiel, S. Cauchetaux, M. Ratner, I. Shapira, C.A. Dinarello, W.E. Paul, IL-1 acts directly on CD4 T cells to enhance their antigen-driven expansion and differentiation, Proceedings of the National Academy of Sciences 106(17) (2009) 7119-7124.

Declaration of interests

☒ The authors declare that they have no known competing financial interests or personal relationships that could have appeared to influence the work reported in this paper.

☐The authors declare the following financial interests/personal relationships which may be considered as potential competing interests: